Urban Climate 68 (2026) 103031

Contents lists available at ScienceDirect

Urban Climate

journal homepage: www.elsevier.com/locate/uclim

Advancing urban atmospheric modeling with coupled mesoscale–LES: A Bologna heatwave case study

Tony Christian Landi [a,*], Daiane Brondani [c], Edoardo Fiorillo [b], Giorgio Veratti [a], Oxana Drofa [a], Fabrizio Roccato [a], Daniela Cava [c], Cinzia De Benedictis [b], Luisa Neri [b], Luca Mortarini [d]

[a] *Italian National Research Council, Institute of Atmospheric Science and Climate, CNR-ISAC, Via Piero Gobetti, 101, 40129 Bologna (BO), Italy*

[b] *Italian National Research Council, Institute of BioEconomy, CNR-IBE, Via Piero Gobetti, 101, 40129 Bologna (BO), Italy*

[c] *Italian National Research Council, Institute of Atmospheric Science and Climate, CNR-ISAC, Strada provinciale Lecce - Monteroni Km 1200 - 73100 Lecce (LE), Italy*

[d] *University of Milano, Department of Earth Sciences "Ardito Desio", Via Mangiagalli 34, 20133, Milano, Italy*

ARTICLE INFO

Dataset link: https://doi.org/10.82214/6AN6-R625

Keywords:
Urban climate
Heatwave
Mesoscale modeling
Large-eddy simulation
Model coupling
High-resolution simulation
Thermal comfort

ABSTRACT

This study presents the first application of a coupled PALM and MOLOCH modeling system over the city of Bologna, Italy, aimed at advancing the understanding of urban-scale meteorology through high-resolution numerical simulations. Focusing on a specific heatwave event in August 2023, which serves as a proxy for increasingly frequent extreme conditions in the Mediterranean basin, we investigate the intricacies of atmospheric dynamics at the micro-scale. A novel software, MOLOCH4PALM, is introduced for preparing initial and time-dependent boundary conditions for PALM by ingesting 3D meteorological fields from the mesoscale MOLOCH model in an offline nesting configuration.

This integration significantly improves the representation of urban atmospheric dynamics, enabling more realistic simulations of temperature patterns and energy exchanges across scales. Validation against observational data collected during the heatwave confirms the reliability of MOLOCH in capturing large-scale temporal variability, despite a consistent cold bias. In contrast, the coarse PALM configuration (50 m resolution) showed poor performance, with low correlation and a pronounced warm bias. Increasing PALM's resolution to 10 m and 2 m corrected these biases, with the 10 m configuration offering the best balance between accuracy and computational efficiency. Additionally, wind speed simulations demonstrated the robustness of the coupled system, particularly under calm wind conditions, highlighting its suitability for urban microclimate studies and heat mitigation planning. Further analysis using multiple linear regression quantified how urban morphology, represented by the Sky View Factor (SVF), and wind speed independently influence 2 m air temperatures across various surface materials. The results revealed distinct diurnal patterns. Higher SVF values increased daytime temperatures due to greater solar exposure but accelerated nighttime cooling through enhanced longwave radiation loss. Conversely, while higher wind speeds promoted cooling during peak insolation, they were linked to warmer nighttime temperatures due to atmospheric mixing. These findings underscore the critical role of urban design in modulating thermal comfort.

* Corresponding author.
E-mail address: tonychristian.landi@cnr.it (T.C. Landi).

https://doi.org/10.1016/j.uclim.2026.103031
Received 24 January 2026; Received in revised form 26 May 2026; Accepted 28 June 2026

1. Introduction

Urbanization has profoundly altered local climate conditions, leading to phenomena such as Urban Heat Islands (UHIs), altered wind patterns, and changes in air quality (Mills, 2014). These changes have significant implications for human health, energy consumption, and environmental sustainability. The combination of population growth, continuous urbanization, and climate change places increasing strain on cities, highlighting the urgency for adaptation strategies and more sustainable urban planning approaches. In particular, the reduction of green spaces due to urban development can exacerbate the effects of UHIs and stresses the importance of integrating green infrastructure in urban planning to mitigate these impacts (Balany et al., 2020), therefore, urban development projects should aim to mitigate the effects of UHIs as much as possible. Building resilient cities requires anticipating the impacts of ongoing challenges, preparing to mitigate their effects, and designing response mechanisms. Vieira Zezzo et al. (2023) pointed out that traditional methodological approaches, such as fieldwork, dominate urban climate studies. They underscore the importance of integrating microscale models in urban climate research to better understand and mitigate the impacts of UHIs. In this context, different types of atmospheric numerical model are used for urban studies (Martilli et al., 2024; Sanchez et al., 2017) ranging from kilometer-scale numerical weather prediction (NWP) models and climate models with integrated urban parameterizations to detailed street-scale models (Wang et al., 2025; Carmeliet and Derome, 2024). Given the different schemes and resolutions, different model groups can provide different answers to the scientific community. In regional climate models, for example, idealized street canyon schemes, which can be useful for simulations of the entire city part of it, are implemented (Pappaccogli et al., 2025; Zonato et al., 2020; Salamanca et al., 2010; Martilli, 2002; Kusaka et al., 2001), due to their relatively low resolution, they can perform simulations on long periods and for large regions (i.e. mesoscale for months or years). On the other hand, there are very high resolution meter-scale models which can provide a detailed picture of individual streets and buildings (Oh et al., 2024; Resler et al., 2024), but due to computational cost they are usually limited in their spatial and temporal scales (i.e. local scale for days or weeks). In general, the heterogeneity of urban landscapes, characterized by varying building heights, street layouts, and land use patterns, poses complexities for both modeling and observational studies. Advances in Computational Fluid Dynamics (CFD) modeling have provided valuable tools to study the high complexity of urban microscale processes (Tominaga et al., 2023). Such models enable researchers to simulate airflow around buildings, pedestrian-level winds, and dispersion of pollutants with high spatial resolution (Belda et al., 2020) taking into account turbulence movements (Maronga et al., 2020). In addition, the need for a more widespread application of these models across various geographical regions is clear to enhance the generalizability of the results. In fact, Urban Climate Models (UCMs) serve as a valuable resource for advancing innovative building technologies that can significantly aid in reducing climate change impacts and enhancing energy efficiency in cities. PALM (Parallelized Large-eddy simulation Model), in which large turbulent eddies are explicitly resolved, is a state of the art UCM that offers the advantage of providing more precise and reliable outcomes than Reynolds-average-Navier–Stokes (RANS) models, as they are capable of capturing three-dimensional temporal variations and airflow patterns around obstacles within urban environments (Zhiyin, 2015). Since a correct definition of urban morphology has been identified as crucial to enhance model performance (Masson, 2006; Stewart et al., 2014), for reliable numerical simulations at the local scale, an adequate fine-scale representation of the urban texture is required. More databases — freely available — can be combined to build highly detailed urban areas; such as OpenStreetMap (https://www.openstreetmap.org, last access: 18 October 2025), NASA Earthdata digital elevation model (DEM; 30 m resolution; global), ESA WorldCover land use classification (10 m resolution; global), GHRSST Level 4 MUR product for sea surface temperature (SST), among others. Recently, Lin et al. (2023) published a free and open source tool, called GEO4PALM, which helps PALM users generate static input files. GEO4PALM is compatible with geospatial data obtained from any source, provided that the data sets comply with standard geoinformation formats and are globally available, with several data sets having a fine resolution of up to 1 m. Alternative procedures are publicly available to generate the necessary geospatial data for realistic PALM simulations (e.g. https://github.com/SebaStad/rPALM)

On the other hand, an accurate representation of boundary conditions, including surface characteristics and atmospheric forcing, is crucial for reliable urban scale simulations (Radović et al., 2024). Significant effort has been put into creating ideal boundary conditions for large eddy simulations, such as those used by the PALM model (Lin et al., 2020; Kadasch et al., 2021; Vogel et al., 2025; Krč et al., 2025). For example, Radović et al. (2024) developed a multimodel ensemble using 16 different configurations of the mesoscale Weather Research and Forecasting (WRF) model to achieve this. Building on this, Lin et al. (2020) developed WRF4PALM, a suite of Python-based tools designed for off-line nesting of the PALM model within the WRF modeling system. Essentially, WRF4PALM generates initial and boundary conditions from WRF output, providing time-varying meteorological forcing for the PALM model. Furthermore, similar efforts have been made to construct initial and boundary conditions for PALM using the output of the COSMO meteorological model (Baldauf et al., 2011) by developing the INIFOR preprocessor (Kadasch et al., 2021). Recently, the PALM-meteo preprocessor (Krč et al., 2025) has been proposed as a modular Python-based tool that prepares PALM dynamic drivers from a variety of mesoscale and global models (WRF, ICON, ALADIN, CAMx, CAMS) and other sources, offering flexible plugin-based import, horizontal regridding, vertical adaptation, and mass-balancing across boundaries. These developments highlight the growing ecosystem of tools for coupling PALM with established mesoscale models. However, the Italian non-hydrostatic mesoscale model MOLOCH, widely used for operational forecasting and research over complex terrain, is not currently supported by PALM-meteo, as its outputs cannot be ingested by the existing preprocessor. This gap motivated the development of a novel interface to enable seamless offline nesting of PALM within MOLOCH.

To advance our understanding of urban-scale meteorology through the development and application of high-resolution numerical models, this study is driven by two main research questions.

Our primary research question is: can the scale gap between a mesoscale model and a microscale Large-Eddy Simulation be effectively bridged to improve urban microclimate predictions? To answer this, we present a novel software, called MOLOCH4PALM,

Table 1
Domain parameters: all domains are centered over the Bolognina district.

	D01	D02	D03
centlat	44.51188	44.51188	44.51188
centlon	11.34641	11.34641	11.34641
nx (grid points)	200	320	500
ny (grid points)	200	320	500
nz (grid points)	60	160	140
dx (m)	50	10	2
dy (m)	50	10	2
dz (m)	50	10	2
ll_x (m)	0	3250	4500
ll_y (m)	0	3250	4500
z_{origin} (m a.g.l.)	0.0	0.0	0.0

to adequately connect the microscale meteorological model with the real atmosphere. The coupling of the PALM model (Maronga et al., 2020) with the state-of-the-art meteorological model MOLOCH (Davolio et al., 2023) is presented by implementing offline nesting. MOLOCH4PALM generates the PALM dynamic drivers, preparing initial and time-dependent boundary conditions by ingesting 3D meteorological fields from MOLOCH. It includes a synthetic turbulence generation method to accelerate the generation of turbulent fluctuations at the boundaries. The present work provides the first modeling application in Italy using a PALM system over the city of Bologna.

Our secondary research question is: how do urban morphology and meteorological drivers independently modulate near-surface temperatures across different urban materials during a heatwave? To address this, we leveraged the high-resolution model outputs to thoroughly investigate the spatial and temporal variability of key microclimatic variables within the innermost simulation domain. Our objective was to quantify the individual influence of urban form, surface type, and wind speed on 2 m air temperature. We used multiple linear regression to analyze the simulated urban microclimate, specifically focusing on these independent impacts throughout the diurnal cycle.

The manuscript is structured as follows: in the Section 2 details of the studied area are reported. Section 3 introduces and describes the MOLOCH4PALM tool's characteristics, alongside the configurations of both the PALM model. Section 4 presents the results of the PALM and MOLOCH comparison against observations, and discusses the spatial and temporal variability of the key microclimatic variables. Finally, Section 5 provides the conclusions drawn from this research.

2. Experiment description

2.1. Study area

The study area is inside Bologna municipality in Italy. With his 387.500 inhabitants Bologna is the largest city in the Emilia-Romagna region. Bologna is known for its medieval architecture and extensive urban heritage, featuring a well-preserved historic center, one of the largest in Europe, with narrow streets, towers, and porticoes dating back to the Middle Ages. Bologna's geography features a transition from northern plains to southern hills, with altitudes in the study area ranging from 15 to 293 m. This varied terrain shapes the city's unique geographical identity, influencing its climate, agriculture, and urban development. Bologna has a humid subtropical climate with continental influences, leading to significant seasonal temperature swings. Summers are hot and humid (25–30°C on average) with occasional highs over 36°C, while winters are cool (0–5°C) with infrequent snowfall. The city experiences large daily and seasonal temperature ranges. Annual rainfall averages 700–800 mm, with peaks in spring and autumn (Antolini et al., 2016; Crespi et al., 2018).

PALM integration domains are centered on the Bolognina district. Located just north of the historic center of Bologna is characterized by a relatively high urban density, with a mix of residential, commercial, and industrial areas. Fig. 1 reports the 3 nested integrations domains together with the weather stations considered for the model assessment.

Domain 01, representing the coarsest resolution, features a uniform horizontal and vertical grid spacing of 50 m, encompassing an 10 km by 10 km square area. Its vertical extent reaches up to 3 km above ground level. Nested within Domain 01, Domain 02 has a resolution to a grid spacing of 10 m, with its upper boundary extending to 1.6 km. The innermost and finest resolution domain, Domain 03, presents an uniform cell-grid dimension of 2 m, covering a 1 km square area. This highly resolved domain focuses on the lower atmospheric layers, with its top boundary at 280 m above ground level. The domain characteristics are summarized in Table 1.

Superimposed on these domains, the figure also delineates the sampling sites used for the verification of the model's temperature predictions. Yellow circles indicate the locations of the CNR-ISAC stations, which include highly accurate temperature and wind speed measurements collected both on a building rooftop and at ground level on a lawn. Green circles denote meteorological stations from the Weather Underground network (www.wunderground.com). These sampling sites provide the observational data against which the PALM model runs are compared to assess their accuracy. The sampling sites characteristics — in terms of location and pavement type on which they are installed — are reported in Table 2. This information is relevant because this study aims to highlight the effect of UHI in the Bolognina area and how the different materials and land cover influence the thermal dynamics

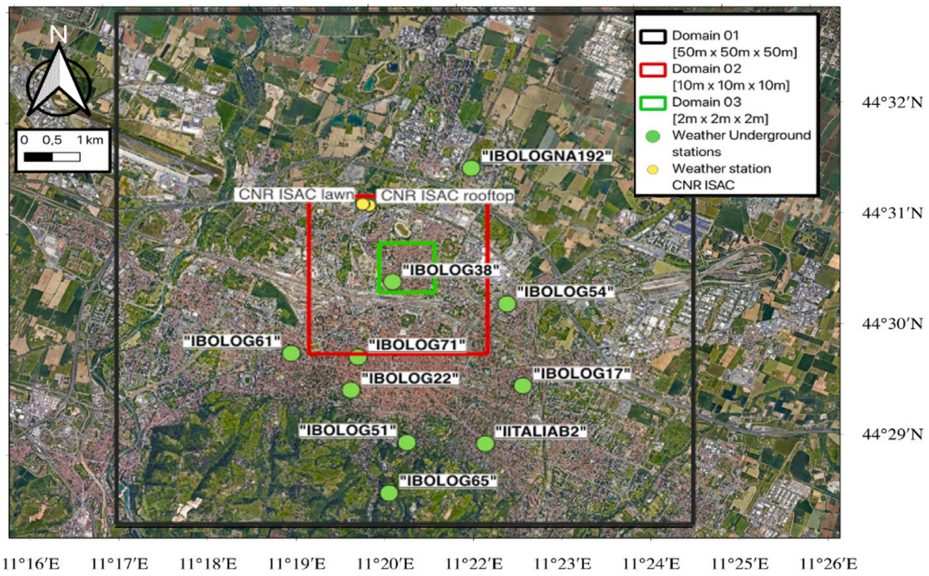

Fig. 1. The integration domains for PALM runs (Satellite image ©2025 Google): *D01* (black solid line) has an horizontal and vertical grid spacing of 50 m and covers a square of 10 km × 10 km. Its vertical grid extends up to 3 km above the ground level; *D02* (red solid line) has grid spacing of 10 m and the top is at 1.6 km; *D03* (green solid line) has a cell-grid dimension of 2 m and covers only the lower atmospheric layers, up to 280 m. It encompasses a total area of 1 km square. Circles indicate the sampling sites used for model runs verification of temperature values. By the yellow circles: CNR-ISAC (yellow) on the building rooftop and at ground level on the lawn. By the green circles the meteorological stations of Weather Underground network downloaded by weatherunderground website.

Table 2
Details of the meteorological stations used in the study, including their name, geographical coordinates (latitude and longitude), UTM32N projected coordinates (easting and northing), and the representative surface type at each location. These stations provide the observational data for model validation and analysis of surface–atmosphere interactions.

Name station	Latitude	Longitude	UTM32N easting	UTM32N northing	Surface type
IBOLOG22	44.490043	11.3332	685 516.7	4 928 951.0	Rooftop
IBOLOG38	44.509598	11.343367	686 262.8	4 931 146.2	Rooftop
IITALIAB2	44.47963	11.363085	687 926.3	4 927 862.6	Rooftop
CNR ISAC 1	44.52362	11.338606	685 839.7	4 932 693.6	Rooftop
IBOLOG65	44.471083	11.34104	686 200.4	4 926 862.7	Grass
IBOLOGNA192	44.52993	11.361944	687 674.0	4 933 447.2	Lawn
CNR ISAC 2	44.52389	11.33721	685 727.9	4 932 719.8	Grass
IBOLOG17	44.49002	11.37198	688 600.2	4 929 037.2	Street level
IBOLOG45	44.50501	11.36900	688 315.0	4 930 695.4	Street level
IBOLOG51	44.480207	11.345448	686 521.9	4 927 886.3	Cement
IBOLOG61	44.49701	11.32001	684 445.9	4 929 695.0	Asphalt
IBOLOG71	44.49602	11.33502	685 642.4	4 929 619.0	Metal

of the urban environment. To provide a quantitative overview of recent/typical air temperature variations observed in bolognina area we show — in Fig. 2 - the monthly air temperature median, 5th and 95th percentiles, calculated over a four-years period (2021–2024) and the median value during the heatwave occurred on August 23rd–24th 2023.

The exceptional warmth of August 24th and 25th, 2023, is clearly evident in the temporal evolution of air temperature at the IBOLOG38 station. During this two-day period, the median temperature markedly exceeded the typical monthly median, reaching the annual maximum. The authors selected this specific event as the focal case study presented in this article.

3. Methodology

3.1. MOLOCH4PALM v1.0 software for dynamic driver

As reported in the recent literature (Radović et al., 2024), time-dependent boundary conditions of the atmosphere are critical for accurate representation of micro-scale meteorological dynamics in high-resolution real-data simulations. In this paper, we report a case study in which the PALM model (Maronga et al., 2020) is integrated within the mesoscale model by defining initial conditions

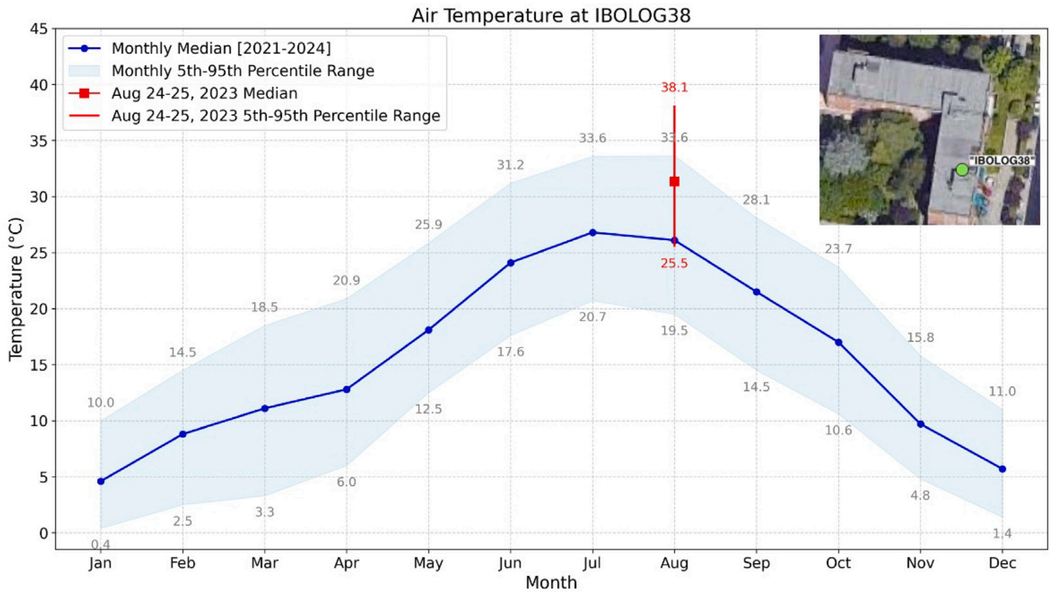

Fig. 2. Air temperature measured at IBOLOG38 measurement station. Monthly median and 5th and 95th percentiles are reported (blue solid line with transparent area) compared with median air temperature computed over 2-days period (red square and vertical red bar, indicating 5th and 95th percentiles), August 24 and 25 2023, in which annual maximum was measured.

and time-dependent boundary conditions. The boundary conditions for PALM are specified for the upper and lateral limits of the domain, while the initial conditions at the surface are provided by PALM's urban and land surface model itself.

A dedicated set of FORTRAN90 routines, named MOLOCH4PALM, has been developed to enable the offline nesting of the PALM urban climate model within the meteorological framework of MOLOCH, developed by CNR-ISAC (Davolio et al., 2023). Since September 2023, the source code of the GLOBO/BOLAM/MOLOCH modeling chain has been made freely available at https://gitlab.com/isac-meteo/globo-bolam-moloch, with installation instructions and documentation accessible via the official web page. The MOLOCH4PALM interface extracts and processes MOLOCH outputs to generate initial and boundary conditions required for PALM simulations, thereby providing time-varying meteorological forcing. This development builds upon the existing INIFOR tool, originally designed for coupling with the COSMO model (Kadasch et al., 2021), and has been adapted to meet the specific requirements of the MOLOCH–PALM system. To address the spatial scale mismatch between the mesoscale and microscale models, the 3D interpolation in MOLOCH4PALM is split into two steps. First, a horizontal bi-linear interpolator maps the variables onto an intermediate grid that shares PALM's horizontal resolution but retains MOLOCH's vertical levels, during which wind vectors are explicitly rotated to match the PALM Cartesian orientation. Secondly, a linear vertical interpolation is performed onto PALM's z-levels. MOLOCH4PALM does not apply a divergence-free correction to the interpolated velocity fields prior to ingestion. Regarding the temporal resolution MOLOCH4PALM strictly follows the output frequency of the mesoscale model, which in this study is 1 h (3600 s). MOLOCH4PALM does not perform any temporal interpolation during the pre-processing stage. PALM reads the hourly boundary data by the dynanic driver and performs a linear temporal interpolation at every computational LES time step. This internal interpolation ensures a smooth, continuous transition of the boundary conditions, preventing numerical instabilities associated with sudden hourly data updates.

Besides, time-varying dynamic boundaries are strictly superior to idealized forcings (e.g., cyclic boundaries with wind profiles) for this real-world case study. Idealized approaches assume infinite fetch and steady-state conditions, failing to capture Bologna's complex regional advection and the non-stationary synoptic transitions of a 48-hour heatwave. MOLOCH4PALM overcomes these limitations by continuously ingesting time-evolving regional weather. This dynamic coupling is essential for accurate, hour-by-hour validation against actual weather stations, ensuring the simulated urban heat island is driven by true atmospheric conditions rather than synthetic approximations.

Fig. 3 illustrates a simplified flowchart of the MOLOCH4PALM software architecture.

This novel software implementation has been applied for the first time to a real-case simulation over the city of Bologna, using the PALM model. The MOLOCH4PALM interface was employed to generate the dynamic driver for the parent domain (D01) of PALM. As a prerequisite, the PALM grid specification must be provided as input during the MOLOCH4PALM.configuration. Following the methodology described by Kadasch et al. (2021), the MOLOCH outputs, with horizontal grid spacing of 1.250 m, are interpolated into the PALM grid cells along the longitudinal (west–east), latitudinal (south-north) and vertical axes, using the respective grid spacings dx, dy, and dz. To correctly position the PALM domain within the MOLOCH domain, the latitude and longitude of the domain center must be specified.

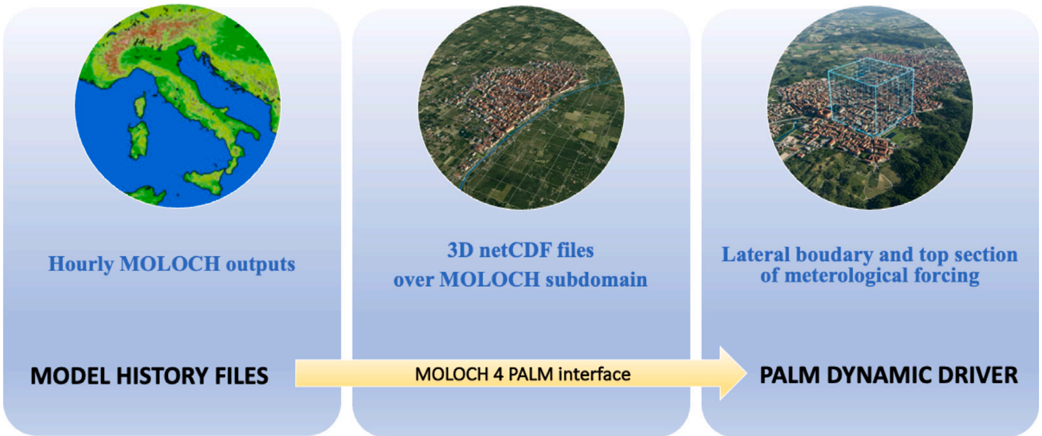

Fig. 3. Schematic flowchart of the MOLOCH4PALM interface. In the left panel, hourly mesoscale meteorological predictions, with an horizontal resolution of 1.250 m, generated by MOLOCH (MHF: Model History File) are converted into NetCDF format over a subdomain centered on the city/area of interest (central panel); these 3D files are then transformed into lateral and top boundary conditions according to the dynamic driver requirements of the PALMmodel (right panel).

Table 3
Variables prepared by MOLOCH4PALM interface for PALM starting from MOLOCH predictions.

Variables	Units
Velocity components (u, v, w)	m s^{-1}
Temperature	K
Geostrophic components (u_g, v_g)	m s^{-1}
Pressure	Pa
Surface pressure	Pa
Specific humidity	kg/kg
Cloud mixing ratio	kg/kg
Soil temperature (multilayer model)	K
Specific volumetric water content of soil	m^3 m^{-3}
Ground temperature	K
Downward diffusive short wave radiation at surface	W m^{-2}
Net short and long wave radiation flux (at the surface)	W m^{-2}
Downward direct short wave radiation at surface	W m^{-2}
2 m temperature	K
Large scale rain (Accumulation)	kg m^{-2}
Large-scale snowfall — water equivalent (Accumulation)	kg m^{-2}
Graupel (snow pellets) precipitation (Accumulation)	kg m^{-2}
Evaporation at surface	kg m^{-2}

The main process implemented in MOLOCH4PALM involves interpolating and extrapolating various meteorological variables from MOLOCH to PALM's grid. As stated above, MOLOCH outputs are interpolated into the PALM grid cells on the lateral and top boundaries for the variables listed in Table 3. The PALM model requires time-dependent dynamic boundary conditions for the three velocity components, potential temperature, and specific humidity. Soil variables are only used for initial land surface model setup, after which the soil model evolves independently. The use of dynamic driver variables depends strictly on PALM namelist settings and activated physical modules. It is worth noting that in mesoscale meteorological models — even those that are convection-permitting — the vertical wind component (w) typically exhibits very low magnitudes, often approaching zero. This behavior is not necessarily indicative of a lack of vertical motion in the atmosphere but rather a consequence of how these models are designed and the physical processes they resolve. Mesoscale models generally parametrize turbulence, meaning that small-scale turbulent motions are not explicitly resolved, but are instead represented through simplified statistical/parametric relationships. As a result, the resolved vertical velocity field lacks the fine-scale variability and intensity that would be present in a fully turbulent flow. This is particularly true in the boundary layer and near-surface regions, where vertical motions are crucial for processes like heat and moisture exchange but are often smoothed out or underrepresented. MOLOCH incorporates a turbulence scheme based on a E-l, order 1.5 closure theory, where the turbulent kinetic energy equation (including advection) is evaluated (Zampieri, 2004). Surface turbulent fluxes of momentum, specific humidity and temperature are computed by the classical Monin-Obukhov theory (Monin and Obukhov, 1954) with Businger/Holtslag functions in the unstable/stable case.

In the context, our efforts are focused on the model coupling MOLOCH/PALM, aiming to calculate the realistic vertical profiles of w to simulate urban turbulence and vertical mixing accurately. On the other hand, on the horizontal plane, bilinear interpolation is

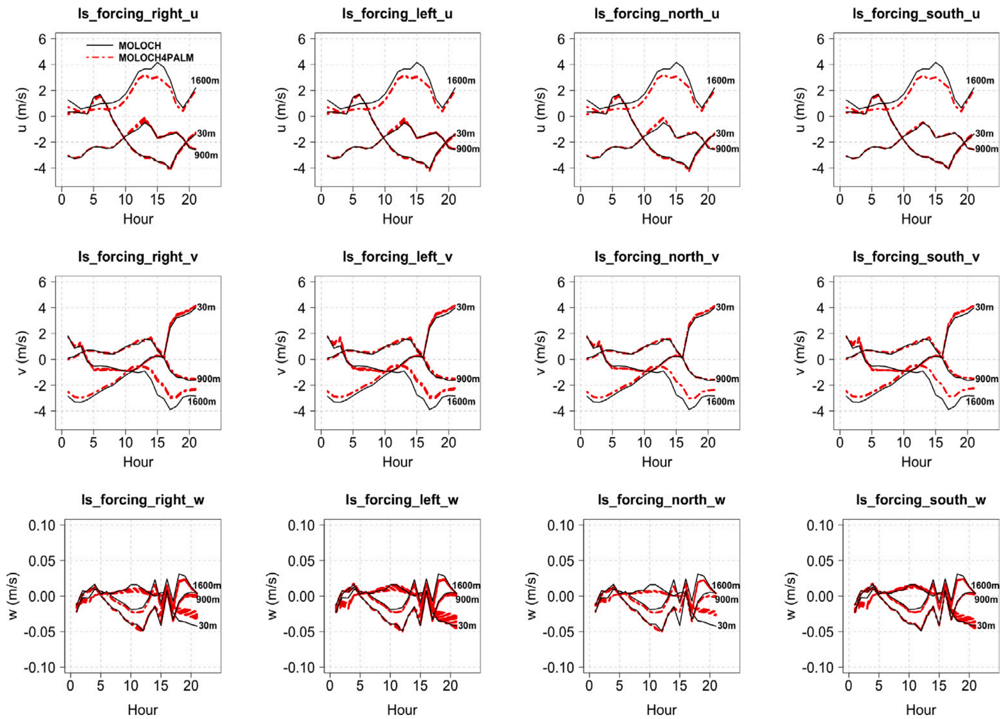

Fig. 4. MOLOCH4PALM verification for the *u*, *v* and *w* wind components at different height, 30 m, 900 m and 1600 m above the ground level. Bilinear interpolation was performed for MOLOCH values (black line) compared all lumped points of the dynamic driver generated by MOLOCH4PALM (red dashed line).

done on each PALM grid vertical level. The MOLOCH model uses a rotated geographic coordinate system for the horizontal grid. In this system, the grid cells are not aligned with the normal geographic coordinate axes. The proper trigonometric functions are used to calculate the MOLOCH grid point coordinates and to convert the vectorial variables into the UTM coordinate system, used by the PALM model. By processing data from a mesoscale model, MOLOCH4PALM software can generate time-varying boundary conditions. This seamless integration allows PALM to dynamically incorporate time-evolving synoptic (mesoscale-scale) weather patterns into its simulations. Consequently, the LES model is equipped to create far more realistic and temporally consistent scenarios, accurately reflecting how changes in regional weather influence local urban conditions (Wang et al., 2023).

In Fig. 4, we report a quantitative comparison of MOLOCH and

MOLOCH4PALM outputs to verify the alignment of MOLOCH prediction with PALM boundary conditions across varying vertical levels. MOLOCH cross sections corresponding to the D01 lateral boundary were extracted and compared with dynamic driver generated by MOLOCH4PALM. Such assessment was done for the wind components, *u*, *v* and *w*. Fig. 4 presents the verification results of the MOLOCH4PALM model for the wind components *u*, *v* and *w* at three distinct altitudes above ground level: 30 m, 900 m, and 1600 m. MOLOCH values were compared against the aggregated boundary data from MOLOCH4PALM, depicted by the orange dashed line.

From Fig. 4, it is evident that the *u* and *v* components show a generally good agreement between MOLOCH and MOLOCH4PALM dynamic driver across all heights, indicating a coherent horizontal wind structure and effective data conversion. The apparent discrepancies in the w wind component are primarily due to the limited range of values represented on the *y*-axis, which spans only from approximately − 0.01 to 0.01. This narrow scale exaggerates even minor differences between the models, making the variations appear more significant than they actually are. Overall, the results confirm that the interpolation method provides a reliable transition of wind fields from MOLOCH to PALM, supporting the robustness of MOLOCH4PALM software. Since turbulence is completely parameterized in MOLOCH, it is also not included in the dynamic driver. Nevertheless, to allow for the realistic development of turbulent structures within the PALM simulation, we designed a case study in which the parent domain (D01) is positioned with sufficient spatial separation from the nested child domain (D02). This setup enables the generation and evolution of turbulence through the Synthetic Turbulence Generator (STG) integrated in PALM, as described by Gronemeier et al. (2015). By leveraging STG, we aim to compensate for the absence of resolved turbulence in MOLOCH and ensure a physically consistent initialization of turbulent flow within the high-resolution urban domain (D03). To bridge the scale gap at the mesoscale-to-LES interface, the built-in PALM Synthetic Turbulence Generator was activated, based on the formulations of Xie and Castro (2008) and Kim et al. (2013). Because explicit high-resolution Reynolds stress data were unavailable at the boundaries, we utilized PALM's automatic parameterization method. The inflow turbulence statistics and the components of the Reynolds stress tensor are parameterized as a function of height based on the local boundary layer state, derived from the friction velocity, Obukhov length,

Table 4
List of input layers and data sources for variables included in the static driver of the child domain.

Variable	Input layers and format	Source
zt	5 × 5 m DEM (raster)	ER Geoportal
building_type	Polygon vector	Municipality of Bologna Geoportal
building_2d	1 × 1 m LiDaR (raster)	Italian Ministry of the Environment
	Polygon vector	Municipality of Bologna Geoportal
building_id	Polygon vector	Municipality of Bologna Geoportal
vegetation_type	Public point vector	Municipality of Bologna Geoportal
	Private point vector	Field survey
	Short grass polygon vector	Photointerpretation
pavement_type	Vector	Photointerpretation
	Vector	Field survey
street_type	Vector	OSM

and the boundary-layer depth calculated via the bulk Richardson criterion (Rotach et al., 1996; Heinze et al., 2017). To capture the continuous evolution of the diurnal cycle and transitions in atmospheric stability, the Reynolds stress tensor is dynamically updated at 30 min intervals throughout the multi-day simulation (Kadasch et al., 2021). The inclusion of the STG is a strict methodological requirement dictated by the domain geometry. The fetch distances from the parent domain (D01) boundaries to the nested urban domains D02 and D03 are 3.25 km and 4.5 km, respectively. Under typical daytime conditions in the Po Valley, where the planetary boundary layer depth can reach up to 2 km, the resulting normalized fetch ranges between 1.6 and 2.25. Because the natural generation of fully developed boundary layer turbulence over heterogeneous urban surfaces typically requires a normalized fetch of approximately 10 (Kim et al., 2013), relying on self-development over these distances would result in unphysical, under-turbulent inflow conditions. The STG effectively bypasses this spatial constraint, ensuring realistic turbulent structures over the urban canopy without requiring computationally prohibitive domain extensions.

In fact, the case studies was designed both to demonstrate the numerical stability of MOLOCH4PALM and to validate meteorology in the simulations, as reported in Section 4.1. The tool is specifically designed to incorporate only the mesoscale atmospheric dynamics provided by MOLOCH, and it does not rely on PALM static driver.

The MOLOCH4PALM software is freely accessible at
https://git.isac.cnr.it/landi/moloch4palm (Landi et al., 2025a). Comprehensive technical documentation, including a detailed user guide with step-by-step instructions for installation and execution, is provided within the software package. This resource is intended to support users in configuring and running the MOLOCH4PALM interface for offline nesting of PALM with MOLOCH outputs.

3.2. Static driver for PALM

As stated above, PALM is an obstacle-resolving model, on a given domain, it can reproduce the near-surface microscale structures by using a static driver file in which information on streets, vegetation, buildings, soil and water bodies are incorporated.

For this study, GEO4PALM software was used for generating the static driver for D01 and D02 (Fig. 1), while ad-hoc procedure — based on rPALM library — was implemented for D03. Regarding D01 and D02, lookup table to convert ESA WorldCover classes to PALM vegetation type, pavement type, building type, water type, and soil type were adopted (see appendix, Table B2 of Lin et al. (2023)). For street type and building morphology,Open Street Maps was implemented. The static driver for domain D03 was constructed using high-resolution geospatial data obtained from multiple sources, as summarized in Table 4. A substantial portion of the geoinformation layers was downloaded from the official geoportal of the Municipality of Bologna (https://opendata.comune.bologna.it/pages/home/). Additional layers, such as those representing private vegetation (e.g., `vegetation_type`) and pavement characteristics (`pavement_type`), were generated through targeted field surveys and photointerpretation of very high-resolution satellite imagery. To integrate and harmonize these heterogeneous datasets, a dedicated workflow was developed using the R programming environment. This procedure enabled the preprocessing and transformation of geospatial data to meet the input requirements of the PALM model. Key variables such as Leaf Area Density (LAD) and surface fractions were derived and incorporated into the final static driver using the rPALM package
(https://github.com/SebaStad/rPALM), which facilitates the generation of PALM static driver from complex urban geodata.

Terrain height was downloaded in 5 m spatial resolution grid format from the Emilia-Romagna Geoportal (ER Geoportal in Table 4). Elevation in D03 ranges between 39 and 45 m a.s.l with a south-north gradient. Building_type, building_id and building_2d variables were derived from vector data available on the Municipality of Bologna Geoportal. Since some building heights were not available, missing data was determined using airborne LiDAR (Light Detection and Ranging) data with 1 m spatial resolution of the Italian Ministry of the Environment (https://gn.mase.gov.it/portale/home). Most buildings measure between 10 and 20 m and the highest one is 30 m tall. To explicitly resolve the complex urban morphology, building geometry in PALM is represented numerically using a 3-D Cartesian topography based on the mask method (Briscolini and Santangelo, 1989), rather than an immersed boundary approach. In this formulation, a 3-D bit array is utilized to flag obstacle cells and surface-adjacent grid points. The standard governing equations are solved across the entire domain, but the respective terms are physically masked (multiplied by

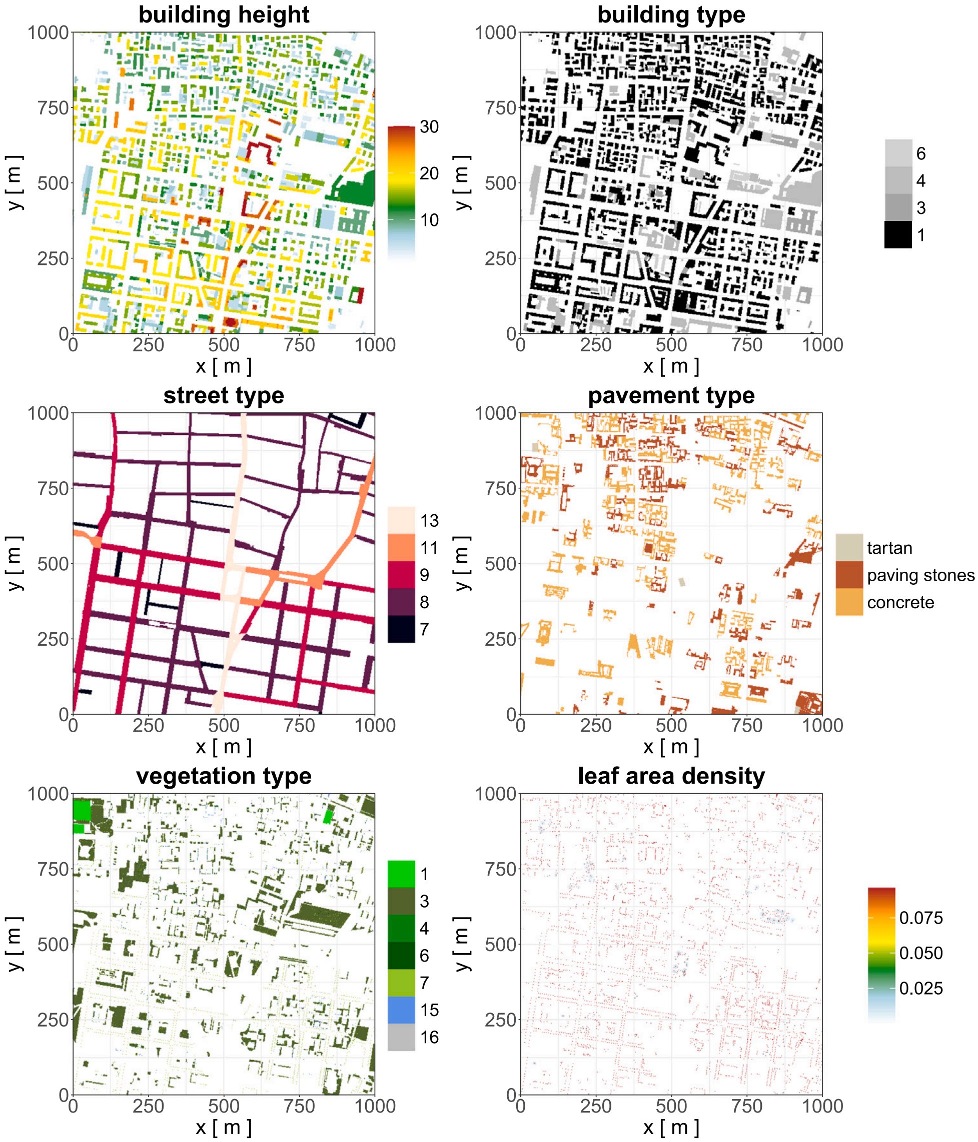

Fig. 5. Main fields included in the static driver for D03.

zero) at the solid obstacle grid points. This method allows for a full 3-D representation of buildings, accommodating even complex or overhanging structures. Regarding the vegetation_type variable, it was determined using three different input layers. For trees, an exhaustive inventory of public and private trees was used, which was developed for a previous study conducted in the same study area (De Benedictis et al., 2025). Briefly, public trees were downloaded in shapefile geoformat from the Geoportal of the Municipality of Bologna. For private trees an ad hoc sampling was carried out in 2023 (July-September). The Qfield app (https://qfield.org/) was customized for tree geolocalization census and storage of the related biometric parameters (species, height, canopy diameter, trunk circumference, canopy shape) required for LAD calculation. Species identification was carried out by botanical experts with the help of the PlantNet app (https://plantnet.org/en/). Short grass areas were identified through photo-interpretation of Googlemaps high resolution imagery. On the whole, seven types of vegetation categories were identified (Fig. 5). Interestingly, among the and 5056 sampled trees, 3189 (63%) are private and 1867 (37%) are public property. The predominance of private green highlights the importance of its inventory.

A portion of the trees was excluded from the static driver for two main reasons: (1) the surface fraction generation process permits only one surface type per grid cell. Following the "BVWP" (Building–Vegetation–Water–Pavement) priority system, tree cells overlapping with building cells were omitted; (2) in cases where multiple trees occupied the same grid cell (typically small private trees), only one tree was included. Consequently, only 4826 trees were successfully incorporated into the static driver for D03. The leaf area density (LAD) and variables were calculated for each tree using the "f.calc_single_tree" function of the rPALM package.

The function is based on the method developed by Lalic and Mihailovic (2004). The pavement_type variable was assessed through photo-interpretation of Googlemaps high resolution imagery and field surveys; 4 different categories of asphalt, concrete and tartan were identified. Street_type was derived from OpenStreetmap (https://www.openstreetmap.org); the child domain includes 5 types of one-way and two-way roads. Since in the child domain there are not water areas, the water_type variable was set to −127 (missing value). On the other hand, since soil grids are not available at high spatial resolution, soil_type variable was assumed horizontally and vertically homogeneous and was set to 3 (medium-fine). In summary, within this 1 square kilometer area, greenery covers 18.95%, while buildings (approximately 10–30 m high, including residential, commercial, and institutional structures) account for 33.35%. The remaining 47.96% consists of asphalt (34.68%), concrete (7.3%), paving stones (5.6%), and a very small portion of tartan (0.13%, possibly indicating an athletics track).

3.3. Model setup

Operational meteorological forecast generated by

GLOBO–BOLAM–MOLOCH modeling system was used for the off-line nesting of PALM. The study area belongs to MOLOCH operational domain (i.e. Italian peninsula), and the description of such meteorological modeling system is reported in Malguzzi et al. (2011). PALM parent domain encompass a 10 × 10 km^2 area centered on the Bolognina district, as outlined in Section 2.1. Isotropic grid spacing is applied across all three domains, and atmospheric processes are resolved up to approximate heights of 3000 m, 1600 m, and 280 m for D01, D02, and D03, respectively. The simulation spans a 48-hour period (two days), corresponding to a heatwave scenario characterized by clear-sky conditions. The run is preceded of a 24 h spinup time to achieve equilibrium conditions of inert soil and wall layer temperature at model initialization, as recommended by Maronga et al. (2020). Virtual measurements not shown here but reported in the provided dataset (Landi et al., 2025b) have been integrated into the model simulations at the measurement stations to improve the quantitative comparison, for further studies, between predictions and ground-level observations (Gronemeier et al., 2021). PALM employs a 1.5-order turbulence closure to directly resolve turbulent motions in the atmospheric boundary layer. SGS turbulence is parameterized following the formulation of Deardorff (1980) as described by Moeng and Wyngaard (1988) and Saiki et al. (2000), with model constant $c\_0 = 0.1$ (Maronga et al., 2015). Near-wall turbulence is represented through a wall model based on Monin Obukhov Similarity Theory applied locally between the surface and the first computational grid level (z = 2 m in D03), as implemented in PALM (Maronga et al., 2020). It uses a multigrid scheme and the FFTW routine to solve the Poisson equation for perturbation pressure at each Runge–Kutta step. Advection terms are discretized with a 5th-order upwind-biased scheme and a 3rd-order Runge–Kutta time-stepping method. Energy balance solvers for buildings and paved surfaces are enabled. For horizontal velocity components and subgrid-scale turbulence kinetic energy, no-slip Dirichlet boundary conditions are applied. The external Rapid Radiation Transfer Model for Global Models (RRTMG) is used for radiation calculations. Data from the non-hydrostatic mesoscale model MOLOCH (Davolio et al., 2023) are used to provide the initial and boundary conditions of time-varying meteorological fields. Static drivers — as described in the Section 3.2 - are implemented for the three different domains. To assess the first implementation of the MOLOCH4PALM modeling system, we plan to conduct a validation by comparing simulated outputs from both MOLOCH and PALM against observational data collected during a heatwave event in Bologna. This validation will focus on evaluating the accuracy of temperature and wind speed predictions across nested domains, with particular attention to the impact of horizontal resolution on model performance. The goal is to quantify the improvements introduced by the multiscale coupling and to verify the system's ability to reproduce urban atmospheric dynamics under extreme thermal conditions.

3.4. Description of the urban microclimate analysis at neighborhood scale

Beyond validating the performance of MOLOCH4PALM, this section details the analytical framework designed to address our secondary research objective: investigating the spatial and temporal variability of the urban microclimate. The selected urban district of Bolognina, characterized by a heterogeneous mix of surface materials, building morphologies, and vegetation types, offered an ideal setting for examining how urban geometry and land cover influence thermal and dynamical atmospheric conditions during a heatwave.

Our specific aim was to quantify the independent influence of urban form, surface type, and local ventilation on near-surface air temperatures. To achieve this, we extracted hourly time series of 2 m air temperature and wind speed from the PALM outputs of the innermost domain (D03, 2 m resolution). These dynamic fields were spatially joined with static classifications of land surface types (e.g., asphalt, concrete, paving stones, vegetation) and with a geometric descriptor of urban canopy openness, the Sky View Factor (SVF). SVF represents the fraction of the sky hemisphere visible from a given point on the ground, unobstructed by surrounding buildings, terrain, or vegetation. It is a dimensionless value ranging from 0 (completely enclosed) to 1 (completely open) and plays a key role in modulating radiative exchanges, ventilation, and thermal comfort in urban environments (Dirksen et al., 2019; Unger, 2009; Daramola and Balogun, 2019). Low SVF values (close to zero), typically found in narrow urban canyons or areas surrounded by tall buildings, reduce incoming solar radiation during the day but also limit longwave radiation loss at night, contributing to elevated nocturnal temperatures and enhanced urban heat island effects. These areas also experience limited natural ventilation. In contrast, high SVF values (approaching one) are indicative of open urban areas such as wide streets or parks, which receive more solar radiation during the day but benefit from more efficient radiative cooling and enhanced air flow at night.

In this study, SVF values were extracted directly from the PALM output using the rtm_skyvft variable. This parameter is calculated internally by the PALM Radiative Transfer Model module, which employs a ray-tracing approach within the model grid to account for

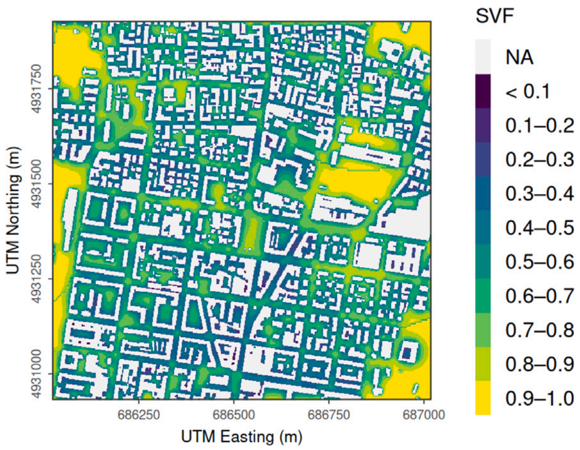

Fig. 6. Ground-level SVF across the domain as computed by PALM.

the shading and masking effects of both buildings and resolved vegetation (Krč et al., 2020). By utilizing the model native SVF output, we ensure that the geometric analysis is fully consistent with the radiative flux computations performed during the simulation.

To focus the analysis on pedestrian relevant environments, SVF data were filtered to include only ground-level horizontal cells not occupied by buildings. The resulting SVF values ranged from approximately zero in deep urban canyons, to one in open plazas or green spaces, as illustrated in Fig. 6.

To assess how urban morphology influences local air temperature while accounting for local ventilation effects, we performed a multiple linear regression analysis. The high-resolution time series of 2 m air temperature extracted from the PALM simulations served as the dependent variable. As explanatory variables, we selected two key predictors, the SVF, representing the radiative openness of the urban canopy, and the wind speed at the lowest model level, which acts as a proxy for near-surface ventilation and convective heat mixing.

Recognizing that surface materials, geometry, and vegetation type strongly modulate microclimatic conditions, we stratified the analysis by both surface classification and hour of the day. Surface classification was derived from the static input raster and includes categories such as asphalt, concrete, paving stones, and vegetation. Hourly stratification was applied to capture the pronounced diurnal variability in radiation load, surface heat exchange and atmospheric stability, which all affect the strength and direction of surface–atmosphere interactions.

For each unique combination of surface type and hour, we applied the linear regression model shown in the Eq. (1):

$$T_a = \beta_0 + \beta_1 \cdot \text{SVF} + \beta_2 \cdot \text{Wind Speed} + \epsilon \quad (1)$$

where T_a is the 2 m air temperature, β_0 is the intercept, β_1 and β_2 are the regression coefficients associated with SVF and wind speed, respectively and ϵ is the residual error term.

This stratified modeling approach enables the isolation of independent contributions of SVF and wind speed to air temperature variations within each land surface type and at different times of day. It also facilitates the detection of surface specific sensitivities, for example, whether vegetation covered areas benefit more from increased ventilation compared to paved surfaces, or whether SVF has a stronger cooling effect under clear sky conditions typical of midday hours.

To ensure model robustness and reliable coefficient estimation, hourly and surface-specific groups with insufficient sample size were excluded from the analysis. This notably included the Tartan surface material, which covered a very limited number of domain cells. The overall explanatory power of the models, as indicated by adjusted R-squared values, and the characteristics of the model residuals, were assessed and presented in Appendix A (Figs. B.13 and B.14). The temporal evolution and statistical significance of each predictor's independent effect were subsequently summarized by extracting and visualizing the estimated coefficients.

Overall, this regression framework provides a concise and interpretable means of quantifying how urban geometry and micro meteorological dynamics interact to shape local thermal conditions at pedestrian level by using physically based outputs of the LES model.

4. Results

4.1. Model validation

We assessed the capability of the PALM model to reproduce urban thermal conditions by comparing its simulated surface air temperatures and wind speed against observations collected in the Bolognina district from August 24 to 25, 2023. This modeling utilized off-line nesting, with the MOLOCH mesoscale model providing the necessary input to drive PALM. The evaluation results are

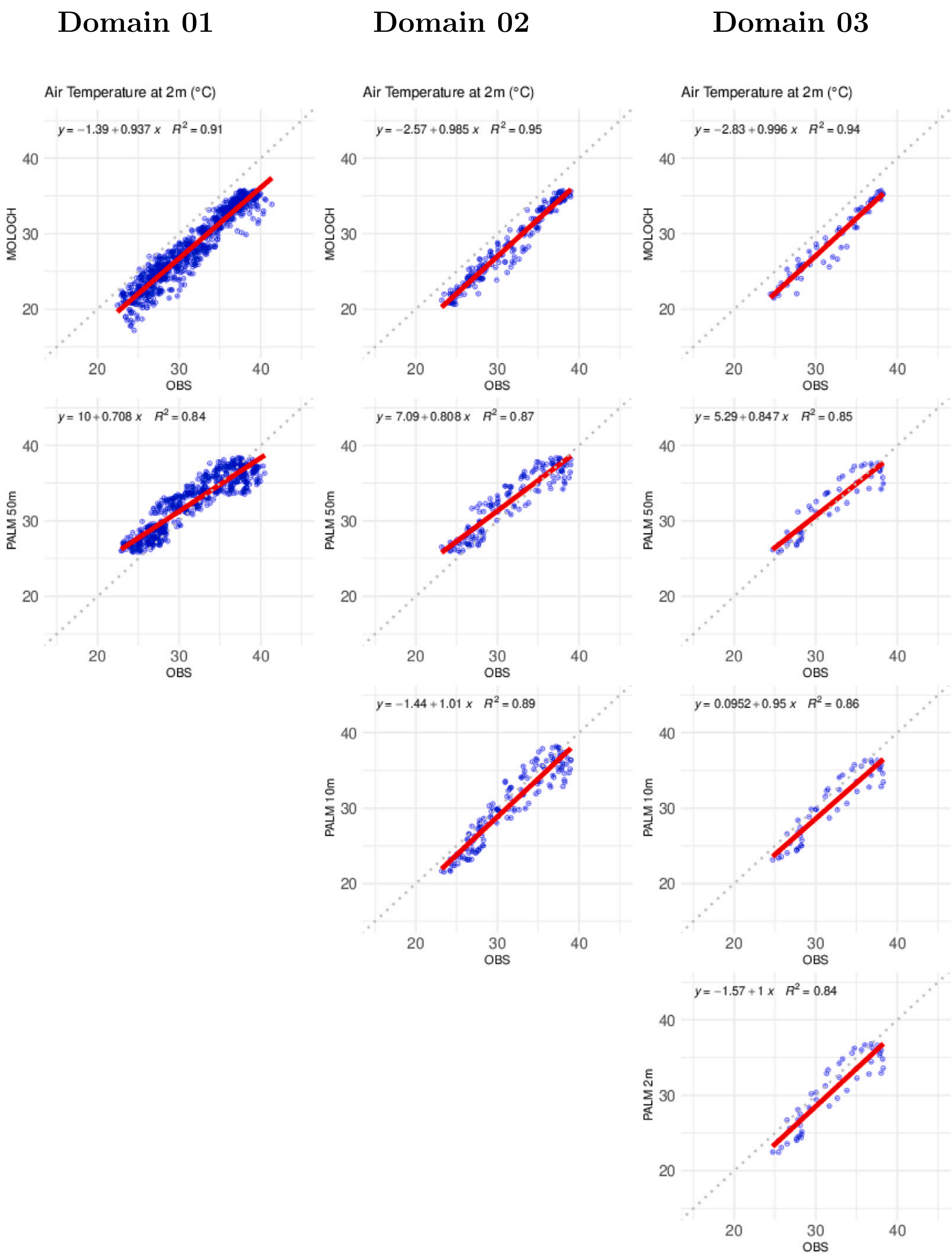

Fig. 7. Scatter plots comparing observed vs. modeled values for different atmospheric model configurations: (first row) MOLOCH, (second row) PALM 50 m, (third row) PALM 10 m, and (fourth row) PALM 2 m. Linear regression line (red solid), its equation, and the correlation coefficient (R^2) are reported. The gray dotted line represents the 1:1 perfect agreement.

visually summarized in the scatter plots of Fig. 7, which compare observed values against the outputs of the standalone MOLOCH run and the three distinct PALM spatial resolutions (50 m, 10 m, and 2 m)

The performance of the models is evaluated based on two key statistical metrics: the slope and intercept of the linear regression $y = a + bx$, which indicate systematic bias, and the correlation coefficient R^2 which measures how well the modeled values explain the variance in the observations. The contrasting biases observed in Fig. 7 can be attributed to specific physical limitations inherent to each model's surface parameterization and resolution. MOLOCH consistently underestimates the observed values, as indicated by the negative intercept of the linear regression based on measurements from the three distinct PALM domains.

The systematic cold bias exhibited by MOLOCH is directly tied to the structural characteristics of its land-surface scheme. As documented by Drofa (2025), MOLOCH categorizes the surface strictly as bare soil, vegetation, or snow, entirely lacking urban parameterization. Consequently, the model cannot represent the thermal properties of impervious urban surfaces. Furthermore, Drofa (2025) highlights that during the warm season, the model tends to systematically underestimate air temperature while overestimating humidity, an error attributed to deficiencies in the computation of the latent heat flux (i.e., excessive evaporative cooling).

Conversely, the PALM 50 m warm bias stems from the spatial resolution, unresolved buildings act as oversized blocks that restrict ventilation and distort shading, artificially trapping sensible heat. Finer resolutions (10 m and 2 m) correctly resolve street topography, restoring realistic aerodynamics and shading to eliminate this bias.

Focusing on the stations within domain D01, MOLOCH achieves a stronger overall statistical fit ($R^2 = 0.91$) compared to the PALM 50 m simulation ($R^2 = 0.84$). Additionally, the PALM 50 m run tends to overestimate nighttime temperatures and underestimate daytime values, further highlighting its systematic *warm bias*. Although MOLOCH retains the highest coefficient of determination (R^2), the transition from PALM 50 m to PALM 10 m represents a substantial methodological advancement. Refining PALM's horizontal resolution from 50 m to 10 m effectively eliminates the pronounced systematic warm bias observed in the coarser setup. The 10 m configuration strikes the best balance between statistical fit ($R^2 = 0.86$) and physical accuracy, with a slope of 0.95 and a near-zero intercept—indicating both improved temperature scaling and minimal bias across the observed range. Increasing PALM's horizontal resolution from 50 m to 10 m and further to 2 m leads to a substantial correction of the warm bias and a marked improvement in temperature scaling. Both the 10 m and 2 m simulations achieve near-perfect linearity, with slopes approaching 1.0, indicating accurate representation of the temperature range. These results underscore the importance of explicitly resolving urban morphology at finer scales. Among the configurations, PALM 10 m often provides the best compromise between computational efficiency and performance, showing the highest correlation with observations in domains D02 and D03. To provide an overview over the site-by-site model assessment, hourly time series of observations, MOLOCH and PALM modeling data are reported in Fig. 8. Both PALM and MOLOCH modeled temperature data represent surface air temperatures.

Such quantitative comparison highlights the model ability to reproduce the diurnal cycle and capture key temperature fluctuations. In particular, MOLOCH time series closely follow the timing of observed temperature peaks and troughs, confirming the model's effectiveness in representing large-scale atmospheric forcing and the 24-hour cycle. Despite a systematic cold bias in absolute values, MOLOCH reliably captures the temporal dynamics of surface air temperature. In contrast, the PALM simulation at 50 m resolution shows a clear inability to accurately reproduce urban thermal conditions. This poor performance is likely attributed to the limitations of the static driver, which inadequately represents fine-scale urban morphology and surface characteristics—resulting in a persistent warm bias and reduced temporal accuracy. However, the time series for the higher-resolution PALM runs (10 m and 2 m) show substantial improvements. The warm bias is nearly eliminated, as the modeled temperature curves for D02 and D03 closely track the observed diurnal variations in absolute magnitude. The higher-resolution runs accurately capture both the daytime peaks and nighttime minima without the persistent overestimation seen in the 50 m setup. These results visually confirm that increasing PALM's resolution is essential for physically realistic temperature magnitudes. The finer grids allow for a more detailed representation of urban geometry and associated energy fluxes, which are critical for capturing the full range of urban thermal variability.

Following the assessment of air temperature, we examined the model's ability to predict wind speed. We present a comparison of wind speed simulations from both MOLOCH and PALM against observational data collected at two specific stations: CNR ISAC 1 (installed on the roof of the building) and CNR ISAC 2 (installed on grass) as depicted in Fig. 9.

The time series of wind speed show good agreement between the modeled data and observations, even under predominantly calm conditions. It is important to note that mesoscale models often struggle to maintain accuracy during low wind regimes, where small-scale turbulence and local effects become dominant. Despite these challenges, the model performs reasonably well in capturing the overall wind speed trends.

Fig. 9 (bottom panels) presents the time series of observed and modeled wind speed at two distinct locations within the study domain: CNR ISAC 1, situated atop an office building, and CNR ISAC 2, located in a grassy area within a small working garden. Observational data are compared against simulations from the mesoscale model MOLOCH and the microscale PALM model, operating at two different resolutions, 50 m and 10 m. Despite the predominantly calm wind conditions observed during the period, with speeds frequently falling below 2 $\mathrm{m\ s^{-1}}$, particularly evident during nocturnal and early morning hours, a generally good agreement is demonstrated between the observational data and the modeled outputs. At CNR ISAC 1, all three models effectively capture the diurnal variability and provide a reasonable representation of the wind speed magnitudes. Similarly, at CNR ISAC 2, the models broadly follow the observed trends, though some minor discrepancies in peak magnitudes or precise timing may be noted, particularly during transitions between calm and slightly elevated wind periods. Table 5 reports the basic statistical metrics reported in Appendix A (correlation coefficient (A.1), mean bias (A.2), and root mean square error (A.3) and) calculated for air temperature and wind speed at CNR ISAC measurement stations.

As stated above, the air temperature results show that MOLOCH consistently achieves very high correlation values at both CNR ISAC stations, indicating strong temporal agreement with observations. However, it tends to systematically underestimate air temperature, as reflected by its negative mean bias and relatively high RMSE. PALM D01 improves upon MOLOCH by significantly reducing the bias and RMSE, although it occasionally overestimates temperatures, especially at the grass site. PALM D02 offers the most balanced performance across both locations, maintaining high correlation while minimizing both bias and error. This suggests

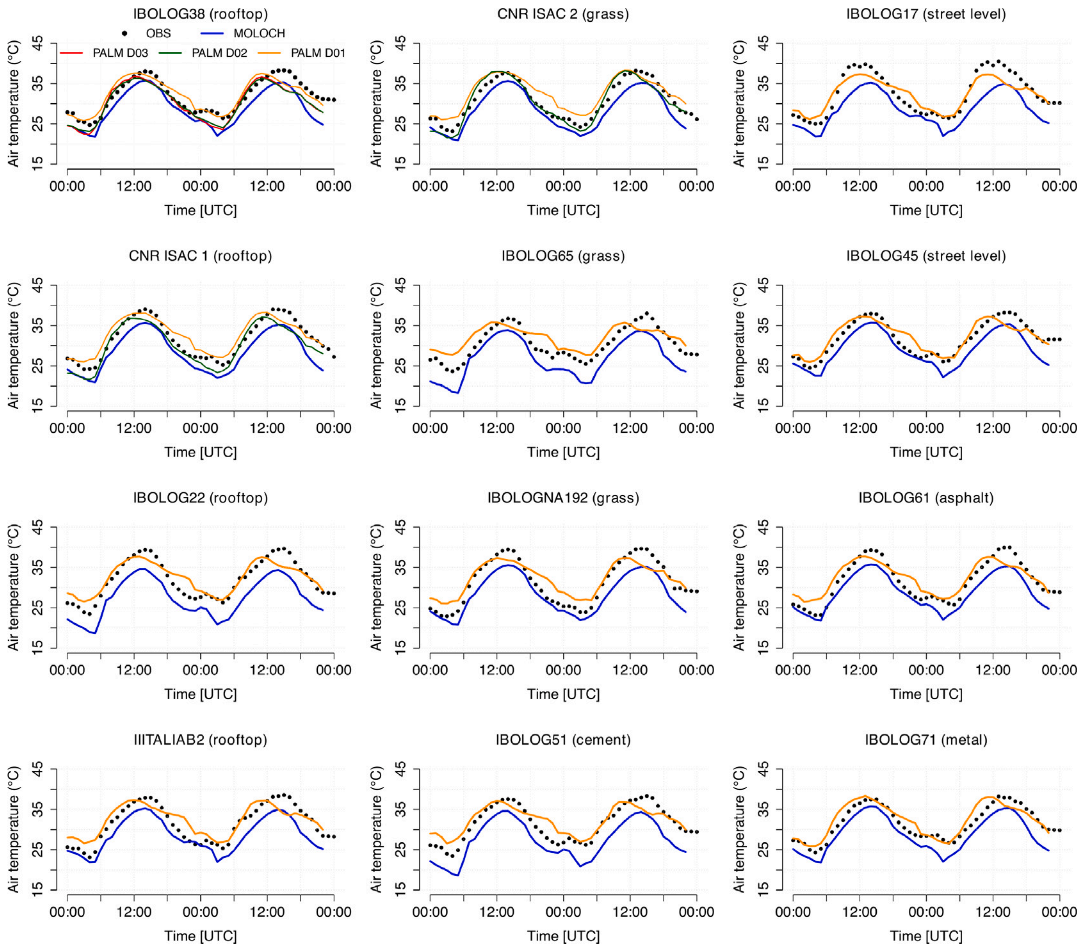

Fig. 8. The time series of simulated air temperature for 00:00 UTC, August 24 and 00:00 UTC and August 25, 2023 compared with observations. In each panel the black dots indicate the measurements, the blue line MOLOCH predictions, the lines orange, green and red depict PALM surface air temperatures calculation with different spatial resolution: D01 refers to 50 m grid spacing, D02 to 10 m and D03 to 2 m - where available (see Fig. 1). PALM simulation covers the 48 h period between August 24 and 25.

Table 5
Basic statistical metrics: correlation coefficient (R), mean bias (MB), and root mean square error (RMSE) calculated for air temperature and wind speed at CNR ISAC measurement stations.

Station name (surface type)	Model	Basic statistics					
		Air temperature			*Wind speed*		
		R	MB	RMSE	R	MB	RMSE
CNR ISAC 1 (rooftop)	MOLOCH	0.98	−3.43	3.80	0.38	−0.36	0.77
	PALM D01	0.94	0.95	1.98	0.44	−0.23	0.82
	PALM D02	0.95	−1.59	2.22	0.49	−0.19	0.79
CNR ISAC 2 (grass)	MOLOCH	0.98	−2.73	2.88	0.41	0.43	0.76
	PALM D01	0.95	1.78	2.31	0.54	0.76	1.09
	PALM D02	0.96	−0.37	1.59	0.46	−0.11	0.44

that PALM D02 provides the most accurate and reliable temperature simulations among the models evaluated. On the other hand, the wind speed results reveal distinct differences in model performance across the two CNR ISAC stations. At the rooftop site (CNR ISAC 1), MOLOCH shows a relatively low correlation of 0.38, with a slight underestimation of wind speed indicated by a mean bias of −0.36 m s^{-1} and an RMSE of 0.77 m s^{-1}. PALM D01 improves the correlation to 0.44 and slightly reduces the bias to −0.23 m s^{-1}, though the RMSE increases marginally to 0.82 m s^{-1}. PALM D02 performs best at this site, with the highest correlation of 0.49, the smallest bias of −0.19 m s^{-1}, and an RMSE of 0.79 m s^{-1}. At the grass-covered site (CNR ISAC 2), MOLOCH again shows moderate

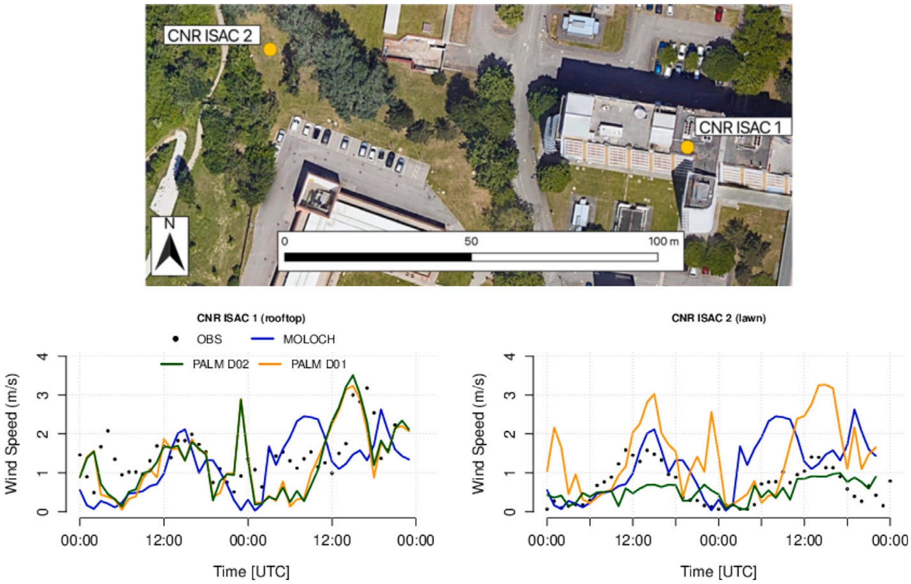

Fig. 9. Upper panel: The locations of the measurement stations CNR ISAC 1 and CNR ISAC 2. Lower panels: The time series of simulated wind speed for 00:00 UTC, August 24 and 00:00 UTC and August 25, 2023 compared with observations, as in Fig. 8.

performance, with a correlation of 0.41, a positive bias of 0.43 m s^{-1}, and an RMSE of 0.76 m s^{-1}. PALM D01 achieves the highest correlation here at 0.54 but also introduces a larger positive bias of 0.76 m s^{-1} and the highest RMSE of 1.09 m s^{-1}. In contrast, PALM D02 offers the most balanced performance, with a correlation of 0.46, a minimal bias of −0.11 m s^{-1}, and the lowest RMSE of 0.44 m s^{-1}. Overall, PALM D02 demonstrates the most consistent and accurate simulation of wind speed across both stations, particularly at the grass site, where it achieves the lowest error and nearly unbiased results.

It is particularly noteworthy that mesoscale models, such as MOLOCH, often face significant challenges and exhibit reduced accuracy specifically during conditions of low or calm wind. These conditions are characterized by weak pressure gradients and complex local flow dynamics that are inherently difficult to resolve accurately at coarser model resolutions. The ability of the coupled model system, especially the nested PALM domains, to capture the observed wind speeds even under these challenging calm conditions, underscores their capacity to resolve localized atmospheric processes crucial for urban microclimate studies (Cava et al., 2025).

4.2. Description of the urban microclimate dynamics

The two-day PALM simulation during a heatwave in northern Italy provides insights into the diurnal variability of 2 m air temperature and surface wind speed within the urban environment of Bologna. Following the validation of the model performances in reproducing the observed trend in the previous section, this analysis focuses on the identification of atmospheric responses influenced by different surface materials and urban morphology.

Fig. 10 panel (a) presents the diurnal cycle of 2 m air temperature observed over asphalt surfaces throughout the two-day simulation (August 24–25). Asphalt was selected as the reference surface due to its pervasive distribution within the domain, excluding building footprints. A clear and characteristic diurnal pattern is observed, with temperatures rising sharply after sunrise, peaking in the early afternoon, and gradually decreasing overnight. The median 2 m air temperature over asphalt reached its maximum values around 12:00–13:00 local time depending on the day, with peaks of approximately 37.4°C on both days, with slightly higher 25th and 75th percentiles for August 25. Conversely, the minimum median temperatures over asphalt were recorded in the early morning hours, reaching about 21.1°C on August 24 at 05:00, and rising to around 23.4°C at the same hours on August 25. The box plots reveal a considerable spread in temperatures across asphalt cells, particularly between 07:00 and 10:00, most likely due to varying shading effects from local obstacles (such as buildings and trees) within the simulation domain, reflecting local variability in urban heating, especially during sun rising hours. Interestingly, there was less pronounced nocturnal cooling on the night of August 25. This indicates higher heat retention, which contributed to overall discomfort on what was observed as the hottest day. This reduced nocturnal cooling suggests a stronger persistence of the urban heat island effect on the second day. Fig. 10 panel (b) presents the median and interquartile range (25th to 75th percentile) of the 2 m air temperature differences of other surface materials (concrete, paving stones, and vegetation) relative to the median 2 m air temperature over asphalt. This plot highlights the varying thermal responses of different surfaces. Vegetation consistently maintained cooler air temperatures compared to asphalt throughout the entire 48-hour simulation. The maximum cooling divergence for vegetation occurred during the peak heating hours

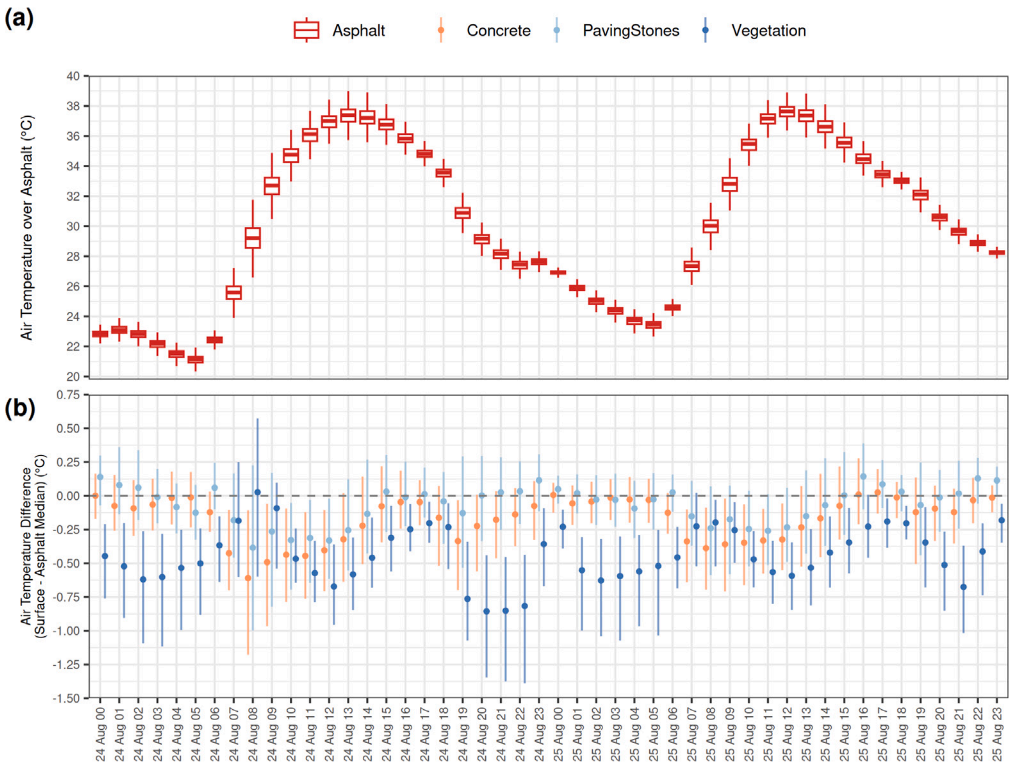

Fig. 10. Diurnal variability of 2 m air temperature during the two-day simulation (August 24–25). Panel (a) illustrates the distribution of 2 m air temperature over asphalt surfaces for each simulated hour. The box plot shows the median (middle horizontal line), 25th percentile (bottom of the box), and 75th percentile (top of the box). Panel (b) presents the median (point) and the 25th to 75th percentile range (vertical line segment) of the 2 m air temperature difference between concrete, paving stones, and vegetation surfaces relative to the median 2 m air temperature over asphalt for each simulated hour.

and also significantly during late night (19:00–22:00) and early morning (01:00–06:00). Specifically, vegetation showed median differences of up to approximately −0.85°C compared to asphalt around 19:00–20:00 on August 24, and values consistently below −0.5°C during the midday and afternoon periods of both days. This significant cooling effect can be attributed to evapotranspiration from vegetative surfaces, which efficiently dissipates incoming solar radiation as latent heat, leading to lower air temperatures.

In contrast, concrete and paving stones exhibited distinct thermal patterns compared to vegetation. During daytime heating, air temperatures over concrete and paving stones were generally close to or slightly cooler than asphalt, with median differences typically within −0.4°C and +0.1°C. For instance, around 10:00–12:00, both concrete and paving stones showed median differences of around −0.4°C to −0.25°C relative to asphalt. The largest divergence among these two surfaces and asphalt occurred in the morning between 07:00 and 13:00, most likely due to their varying thermal inertia and albedo characteristics. Concrete and paving stones, having different thermal properties from asphalt, might heat up at slightly different rates or reflect solar radiation differently during the morning transition, leading to temporary discrepancies in air temperature. During the night, paving stones frequently resulted in slightly warmer air temperatures compared to asphalt, with median differences reaching up to +0.14°C. This nocturnal warming over paving stones is likely due to the slower release of stored heat from these materials, contributing to the urban heat island effect during stable night-time conditions. Conversely, concrete and paving stones showed their closest agreement with asphalt temperatures during the afternoon and the second half of the night when materials tend to reach a more stable thermal equilibrium, having either absorbed their maximum heat during the day or released a significant portion of it overnight.

Between 06:00 and 09:00, concrete and paving stones show their maximum divergent behavior with discrepancies between the median that range between 0.15 and 0.3°C. This can be likely attributed to the different radiative and thermal properties of these materials, such as their specific heat capacity, thermal conductivity, and emissivity, which prompt their rates of heating and cooling following sunrise and during the early morning transition from nocturnal cooling to diurnal heating.

Fig. 11 presents the spatial distribution of 2 m air temperature and 2 m wind speed at the first model layer for three distinct and contrasting situations. The top panels illustrate the conditions at the hottest hour of the simulation, August 25 at 12:00 local time. The middle panels depict the colder conditions observed on August 24 at 05:00 local time. Finally, the bottom panels display an intermediate situation, representing the transition from day to night on August 24 at 22:00.

At the hottest hour of the simulation, August 25 at 12:00 local time, 2 m air temperature (top-left panel) exhibited the strongest spatial gradient among the situations presented here, ranging primarily from approximately 36°C to over 40°C. Only a few grid cells recorded temperatures below 30°C, a phenomenon typically observed in persistently shaded areas or deep recesses formed by building corners, which receive minimal direct solar radiation throughout the day (though not shown in the plot due to scale resolution limitations). Maximum temperature peaks were predominantly observed in areas characterized by generally higher sky view factors, such as large expanses of impervious surfaces. These areas, due to their greater openness to the sky, tend to experience higher 2 m air temperatures during daytime hours because of more direct solar radiation exposure. Conversely, minimum temperatures were evident over larger green spaces, such as parks and areas with substantial tree cover, clearly highlighting the localized cooling effect of vegetation through evapotranspiration. The corresponding 2 m wind speed map for August 25 at 12:00 (top-right panel) shows values ranging from near zero to over 2.8 $m\ s^{-1}$. Higher wind speeds were prevalent in wider and unobstructed streets, where flow channeling occurs or obstacles are minimal. In contrast, street canyons and the leeward sides of buildings exhibited significantly reduced wind speeds, often below 0.4 $m\ s^{-1}$, indicating areas of recirculation and sheltering within the urban canopy layer.

For comparison, the spatial maps for the hour of minimum median 2 m air temperature, August 24 at 05:00 local time, provide a contrasting view. At this hour, 2 m air temperature (middle-left panel) ranged approximately from 19°C to 23°C. While the overall temperatures are considerably lower than midday, the spatial pattern of higher temperatures over built-up areas and cooler temperatures over green spaces persisted. This indicates the continued presence of the nocturnal urban heat island effect, albeit with a significantly reduced magnitude compared to peak daytime hours, as buildings gradually release their stored heat. The 2 m wind speed map for August 24 at 05:00 (middle-right panel) shows significantly lower wind speeds across the entire domain, typically ranging from zero to 0.6 $m\ s^{-1}$. This overall reduction in wind speed is characteristic of stable atmospheric conditions common during nighttime and early morning hours, which reduce turbulent mixing within the urban boundary layer.

The third situation, presented in the bottom panels, is representative of early night conditions, marking the transition from evening cooling to deeper nocturnal processes on August 24 at 22:00. In these hours, the spatial gradients between different urban elements become more evident than during the peak daytime or early morning minima. Vegetation surfaces highlight their strong cooling influence compared to other surfaces, exhibiting colder temperatures by 1–2°C compared to impervious surfaces, with absolute temperatures generally ranging between 24.5 and above 28.5°C. The corresponding 2 m wind speed map for August 24 at 22:00 (bottom-right panel) exhibits very low values, similar to those found during the early morning at 05:00 local time before sunrise. Wind speeds across the domain typically range from zero to 0.4 $m\ s^{-1}$, confirming the dominance of stable atmospheric conditions as the evening progresses. Within this weak flow, areas of highly reduced wind speeds are still distinctly visible within narrow street canyons and immediately downwind of larger building structures, while slightly higher speeds may occur over more open areas with less obstruction.

The previous discussion of spatial temperature maps highlighted the heterogeneous thermal landscape of urban environments. To further quantify the factors driving these observed temperature variations, we performed a multiple linear regression analysis. This investigation provides a detailed quantification of how urban morphology, specifically through the SVF and near-surface wind speed, independently influences 2 m air temperature across different urban surface materials and throughout the diurnal cycle. By stratifying the analysis by surface type and hour, we can identify surface-specific sensitivities and the varying strength and direction of these relationships.

Fig. 12 illustrates the temporal evolution of the estimated regression coefficients for 2 m Wind Speed and SVF for asphalt, concrete, paving stones, and vegetation across the two simulated days. While the standard error for each coefficient estimate was consistently small (ranging from 0.002 to 0.075°C, with a median of 0.016), confidence intervals were omitted from the plot to avoid visual clutter. Nevertheless, it is important to note that the 95% confidence interval crossed the zero line in very few instances. For wind speed, this occurred at 11:00, 17:00 and 19:00 local time on August 24 for concrete, asphalt and vegetation and concrete, respectively, and at 01:00 on August 25 (for paving stones). For SVF, the confidence interval crossed zero only at 00:00 on August 25 for concrete.

A clear diurnal pattern is observed for the influence of both SVF and 2 m wind speed on 2 m air temperature. During daytime hours, generally from 06:00 to 19:00 local time, the coefficients for SVF (Fig. 12, right column) are predominantly positive for all surface types. This indicates that a higher SVF, implying greater openness to the sky and thus more direct solar radiation exposure, leads to higher 2 m air temperatures during the day. These positive coefficients were consistently statistically significant across all surface types and hours of strong solar forcing (p-value < 0.05), with few exception for asphalt at 06:00 on August 24 and concrete at 12:00, 14:00 and 16:00 on August 25, which resulted in a p-value of 0.16, 0.051, 0.14 and 0.078, respectively (see also Fig. B.15). The mentioned effect is particularly strong in the late morning, with coefficients peaking between 08:00 and 09:00 local time, reaching values of the regression coefficient between 2.5 and 3.6°C per unit of SVF on August 24 and between 1.1 and 1.9°C per unit of SVF on August 25 across all impervious surfaces (asphalt, concrete, paving stones). This strong positive correlation highlights the critical role of urban geometry in modulating solar heat gain, where less obstructed areas accumulate more sensible heat. Conversely, during nocturnal hours, from approximately 22:00 to 05:00 local time, the SVF coefficients become negative for all surfaces, suggesting that a higher SVF is associated with lower 2 m air temperatures. These negative coefficients were also found to be largely statistically significant (p-value < 0.05), with exceptions only for concrete at 00:00 on August 25 (Fig. B.15). The negative regression coefficients are attributed to enhanced longwave radiation loss to the cold night sky from more open areas, facilitating more efficient cooling. Vegetation exhibits a similar diurnal pattern, although its SVF coefficients can be smaller in absolute terms, especially during the night, likely influenced by the complex radiative properties and evaporative cooling processes within its canopy.

The influence of 2 m wind speed, serving as a proxy for local ventilation and convective mixing, also displays a pronounced diurnal variation (Fig. 12, left column). During hours of maximum insolation, approximately 12:00 to 17:00 local time, the

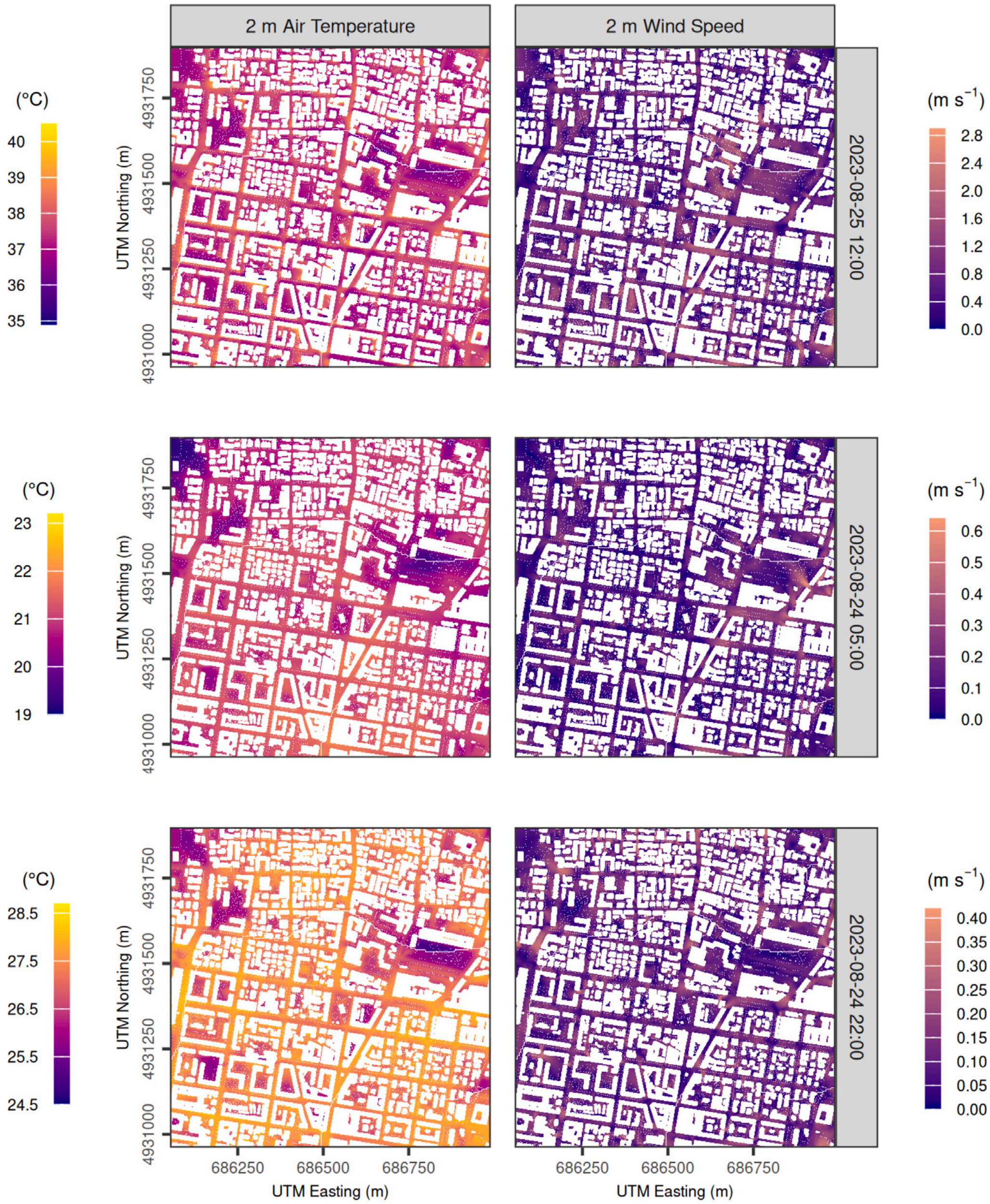

Fig. 11. Spatial distribution of 2 m air temperature (left column) and 2 m wind speed (right column) from the PALM simulation for three characteristic periods during the heatwave. The top row illustrates conditions at the hottest hour (August 25, 12:00 local time), the middle row depicts the coldest hour (August 24, 05:00 local time), and the bottom row shows an intermediate early-night situation (August 24, 22:00 local time).

coefficients for 2 m wind speed are slightly negative for all surface types. Many of these negative coefficients, particularly during August 25, were statistically significant (p-value < 0.05, Fig. B.15). This indicates that higher wind speeds promote a cooling effect, as increased ventilation effectively removes accumulated heat from urban surfaces, leading to lower 2 m air temperatures, with very similar impacts observed across all surfaces.

Starting from 18:00 to approximately 04:00 local time, the coefficients for 2 m wind speed are largely positive for all surface types, with magnitudes dependent on the surface type and hour. This implies that higher wind speeds are associated with higher 2 m air temperatures. This phenomenon can be attributed to increased mixing of warmer air from aloft or advection of warmer air into typically cooler, sheltered spaces close to the surfaces at night. Between 04:00 and 05:00 local time on August 24 and from 00:00 to 05:00 on August 25, it is likely that upper air layers have reached similar temperatures to the ground, and thus the wind speed no

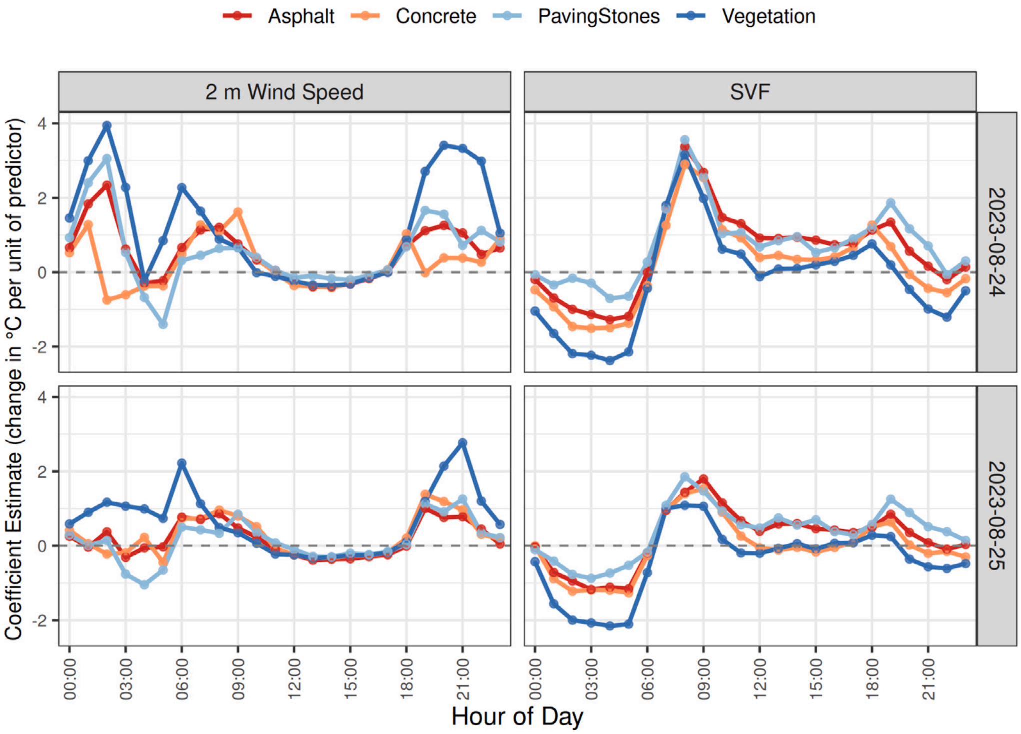

Fig. 12. Estimated regression coefficients representing the independent influence of 2 m Wind Speed (WS, in m s^{-1}) and SVF (dimensionless) on 2 m air temperature (°C) for impervious (Asphalt, Concrete, Paving Stones) and vegetated surfaces. The coefficients are derived from separate hourly-stratified multiple linear regression models, fitted for each surface type and hour of the day. The analysis is presented for two simulated days, August 24 (top row) and August 25 (bottom row), 2023. Positive coefficients indicate a warming effect, while negative coefficients indicate a cooling effect. The dashed gray line indicates a zero coefficient.

longer primarily contributes to the transport of hotter air from above, resulting in regression coefficients close to zero. Vegetation surfaces occasionally show some of the largest positive coefficients for wind speed during night time, sometimes peaking above 3.0°C per m s^{-1}. This could suggest that for vegetation, increased wind speed might facilitate the advection of warmer ambient air into the cooler vegetative canopy, or that highly ventilated vegetated cells are inherently more exposed to overall warmer atmospheric conditions, despite their potential for evaporative cooling.

These results underscore the complex interplay between urban geometry and micrometeorological dynamics in shaping the pedestrian-level thermal environment. They highlight distinct sensitivities of different surface materials to radiative and convective processes throughout the day, providing quantitative insights into the drivers of the spatial temperature patterns previously discussed.

While the regression models effectively captured the distinct and statistically significant influences of SVF and wind speed, it is important to acknowledge the overall model fit and residual characteristics. The adjusted R-squared values for the hourly and surface-specific models were generally modest, often remaining below 0.4, with some exceptions up to 0.6 (Fig. B.13). Such values are, however, common in the analysis of complex environmental processes like urban microclimates, where numerous unmodeled factors, inherent variability, and stochastic atmospheric dynamics contribute to temperature fluctuations. Similarly, while the model residuals generally centered near zero, indicating no systematic over- or under-prediction, some deviations from perfect normality and slight biases were observed (Fig. B.14). These characteristics suggest that a simple linear model, by its nature, may not fully capture the intricate non-linear relationships or higher-order interactions present in natural processes, nor account for all unmeasured drivers of 2 m air temperature. Nevertheless, the robustness and consistent diurnal patterns of the significant regression coefficients for SVF and wind speed provide valuable quantitative insights into their independent roles in shaping the thermal environment. Future investigations could explore more advanced non-linear modeling techniques or incorporate additional environmental variables to enhance the overall explanatory power and refine the capture of complex atmospheric interactions.

5. Conclusions and outlooks

By developing and employing the novel MOLOCH4PALM software for offline nesting, we establish a robust multiscale framework that effectively couples the mesoscale MOLOCH model with the microscale PALM model. This integration significantly enhances the representation of urban atmospheric dynamics, allowing for a more physically realistic simulation of temperature patterns and energy exchanges across scales. The results demonstrate the potential of MOLOCH4PALM to bridge mesoscale forcing with high-resolution urban climate modeling, offering a valuable tool for future urban climate studies and heat mitigation strategies. To assess the performance and reliability of the modeling system, a validation was carried out by comparing simulated outputs from MOLOCH and PALM against observational data collected during the heatwave event on August 24–25, 2023 in Bologna.

The standalone MOLOCH mesoscale model consistently achieved the highest correlation coefficients ($R^2 = 0.91$ to 0.95), indicating a strong temporal correlation with observed temperature. This performance confirms MOLOCH's reliability in capturing large-scale atmospheric forcing and the temporal variability of the diurnal temperature cycle. The regression analysis further supports this, with slopes close to 1.0, demonstrating excellent temperature scaling. However, the model exhibits a consistent cold bias, reflected in the negative intercepts, suggesting a systematic underestimation of absolute temperature values. The coarse PALM configuration with 50 m grid spacing exhibited notably poor performance. It was associated with the lowest correlation coefficients (R^2 values as low as 0.84) and, more critically, a pronounced systematic warm bias, as indicated by large positive intercepts (up to 10.00 in domain D01). This substantial offset underscores the inadequacy of the 50 m resolution in resolving key physical processes within the urban canopy layer. The inability to capture fine-scale urban morphology and surface heterogeneity leads to significant errors in the simulation of absolute temperature magnitudes.

One of the most significant findings of this study is the substantial improvement in model performance achieved by increasing the horizontal resolution of PALM. Transitioning from 50 m to 10 m and 2 m effectively corrected the major systematic warm bias observed in the coarser configuration. The higher-resolution runs yielded regression slopes near or exactly 1.00, indicating accurate scaling of the diurnal temperature range, and intercepts close to zero, reflecting minimal bias in absolute temperature values. Among these, the 10 m configuration consistently provided the best statistical balance maintaining strong correlation with observations while nearly eliminating the warm bias. The 2 m run confirmed the perfect scaling behavior but introduced a slight cold offset, similar to that observed in the MOLOCH model, likely due to enhanced sensitivity to local surface features and energy fluxes at very fine scales. Among the tested configurations, PALM 10 m consistently offers the best trade-off between computational efficiency and model performance, achieving the highest correlation with observational data in domains D02 and D03.

The MOLOCH–PALM modeling system demonstrates good overall agreement between simulated and observed wind speeds, a result that is particularly noteworthy given the predominantly calm wind regime during the study period, with speeds frequently below $2\,m\,s^{-1}$. This is a critical aspect of model evaluation, as mesoscale models like MOLOCH often struggle under low-wind conditions, where small-scale turbulence and weak pressure gradients dominate local flow dynamics. The ability of the coupled system to maintain reasonable accuracy under these challenging conditions underscores its robustness and suitability for urban microclimate studies, especially in scenarios characterized by limited atmospheric mixing. These results underscore the value of fine-scale modeling in capturing the dominant drivers of atmospheric behavior under calm conditions, where traditional mesoscale approaches often fall short.

Beyond model validation, our high-resolution PALM simulation provided critical insights into the complex urban microclimate dynamics during the heatwave, highlighting the heterogeneous thermal landscape of Bologna. Analysis of 2 m air temperature across different urban surfaces revealed a clear diurnal cycle, with asphalt surfaces serving as a reference, peaking at approximately 37.4°C in the early afternoon on both August 24 and 25. Surface material significantly modulated these temperatures, with vegetation consistently maintaining cooler air temperatures compared to asphalt (up to about −0.85°C difference), most likely due to evapotranspiration. Conversely, concrete and paving stones showed more varied responses, generally heating similarly to asphalt during the day but occasionally exhibiting slight nocturnal warming. Spatial temperature maps further emphasized these material-specific effects, with maximum temperatures consistently found over large expanses of impervious surfaces with high sky view factors (SVF), while minimums occurred over green spaces, underlining the localized cooling effect of vegetation.

Furthermore, we used a multiple linear regression to quantify the independent roles of urban morphology (through the SVF) and ventilation (through near-surface wind speed) in shaping 2 m air temperature. Our investigation revealed a clear, statistically significant diurnal pattern for the SVF, demonstrating its heating influence during the day and cooling effect via enhanced longwave loss at night. The analysis also revealed the cooling effect of ventilation during peak insolation hours, offering quantitative insights for targeted urban heat mitigation strategies.

In conclusion, this study validates the efficacy of coupling a state-of-the-art mesoscale model like MOLOCH with an LES model like PALM for high-resolution urban meteorological modeling. The substantial reduction in bias and errors achieved by the coupled system highlights its potential to provide more reliable input for urban planning, air quality management, and climate change adaptation strategies, especially in the context of increasing heatwave frequency. Future work should focus on extending this analysis to longer periods and diverse meteorological conditions to further validate the system's robustness, and could explore more advanced non-linear modeling techniques or incorporate additional environmental variables to enhance overall explanatory power and refine the capture of complex atmospheric interactions.

CRediT authorship contribution statement

Tony Christian Landi: Writing – review & editing, Writing – original draft, Visualization, Validation, Supervision, Software, Methodology, Investigation, Funding acquisition, Formal analysis, Data curation, Conceptualization. **Daiane Brondani:** Writing – review & editing, Investigation, Formal analysis, Data curation, Conceptualization. **Edoardo Fiorillo:** Writing – review & editing, Writing – original draft, Visualization, Software, Methodology, Investigation, Formal analysis, Data curation. **Giorgio Veratti:** Writing – review & editing, Visualization, Investigation, Formal analysis, Data curation. **Oxana Drofa:** Software, Resources. **Fabrizio Roccato:** Software, Resources. **Daniela Cava:** Writing – review & editing, Formal analysis, Data curation. **Cinzia De Benedictis:** Data curation. **Luisa Neri:** Data curation. **Luca Mortarini:** Writing – review & editing, Writing – original draft, Visualization, Validation, Supervision, Methodology, Investigation, Formal analysis, Data curation, Conceptualization.

Code availability

The current version of the MOLOCH4PALMv1.0 interface is available from the Institute of Atmospheric Sciences and Climate at https://doi.org/10.82214/Y9XG-CN09 (Landi et al., 2025a).

Data availability

The version of the MOLOCH-PALM outputs used in this study, along with the input data and scripts required to run the PALM model and reproduce all simulations, elaborations, and figures presented in the manuscript, is archived at https://doi.org/10.82214/6AN6-R625 (Landi et al., 2025b).

The Authors would like to clarify that the dataset and the software version described and used in the manuscript has been archived in the CNR-ISAC Archive Data Center, which is a certified long-term and persistent repository, comparable to Zenodo or Figshare. This repository is officially registered in re3data, guaranteeing sustainability and accessibility over time. Further details can be found at the following link: https://www.re3data.org/repository/r3d100014692. This ensures that the archived version of the software remains permanently accessible and citable, in full compliance with the most of journal's requirements. Please do not hesitate to contact us should you require additional information or documentation regarding the repository or the archived version.

Declaration of generative AI and AI-assisted technologies in the manuscript preparation process

During the preparation of this work, the authors used Copilot to review English grammar. After using this tool/service, the authors reviewed and edited the content as needed and assume full responsibility for the content of the published article.

Funding

This research has been supported by the European Union NextGenerationEU programme through two major grants: The National Biodiversity Future Center (NBFC) Project (Code CN00000033, Concession Decree No. 1034 of 17 June 2022) funded under the National Recovery and Resilience Plan (NRRP), Mission 4 Component 2 Investment 1.4 – Call for tender No. 3138 of 16 December 2021, rectified by Decree n. 3175 of 18 December 2021 of Italian Ministry of University and Research; and The Ecosystem for Sustainable Transition in Emilia Romagna (ECOSISTER) project (grant No. ECS00000033, award no. 0001052, dated 23 June 2022) under the National Recovery and Resilience Plan (NRRP; Mission 4, Component 2, Investment Line 1.5: "Establishing and strengthening" of "innovation ecosystems for sustainability", building "territorial leaders of R&D").

Declaration of competing interest

The authors declare that they have no known competing financial interests or personal relationships that could have appeared to influence the work reported in this paper.

Acknowledgments

The authors gratefully acknowledge the CINECA High Performance Computing (HPC) facility for providing the computational resources and support for this project. This work was conducted under the AUSM-LES and IMPACTA projects of the ISCRA-C program, within the science domain of Earth and Climate Science. Computational resources at CINECA for this work have also been funded by UNITECH INDACO, which is an HPC project at the state University of Milan (Italy). The authors acknowledge the use of Copilot AI in the preparation of this manuscript. As none of the authors are native English speakers, generative Artificial Intelligence (AI) tools were employed to assist with grammar correction and to enhance the writing style. However, the overall contribution of AI to the manuscript remained below 10%.

Appendix A. Formulas of statistical indices

$$\text{Correlation Coefficient (R)} = \frac{\sum_{i=1}^{N}(P_i - \bar{P})(O_i - \bar{O})}{\sqrt{\sum_{i=1}^{N}(P_i - \bar{P})^2}\sqrt{\sum_{i=1}^{N}(O_i - \bar{O})^2}} \tag{A.1}$$

$$\text{Mean Bias (MB)} = \frac{1}{N}\sum_{i=1}^{N}(P_i - O_i) \tag{A.2}$$

$$\text{Root Mean Square Error (RMSE)} = \sqrt{\frac{1}{N}\sum_{i=1}^{N}(P_i - O_i)^2} \tag{A.3}$$

where:

- N = number of observations
- P_i = predicted (simulated) value at observation i
- O_i = observed value at observation i
- $\bar{P}$ = mean of predicted values
- $\bar{O}$ = mean of observed values

Appendix B. Model diagnostics and performance metrics

See Figs. B.13–B.15.

Data availability

The version of the MOLOCH-PALM outputs used in this study, along with the input data and scripts required to run the PALM model and reproduce all simulations, elaborations, and figures presented in the manuscript, is archived at https://doi.org/10.82214/6AN6-R625 Landi et al. (2025b).

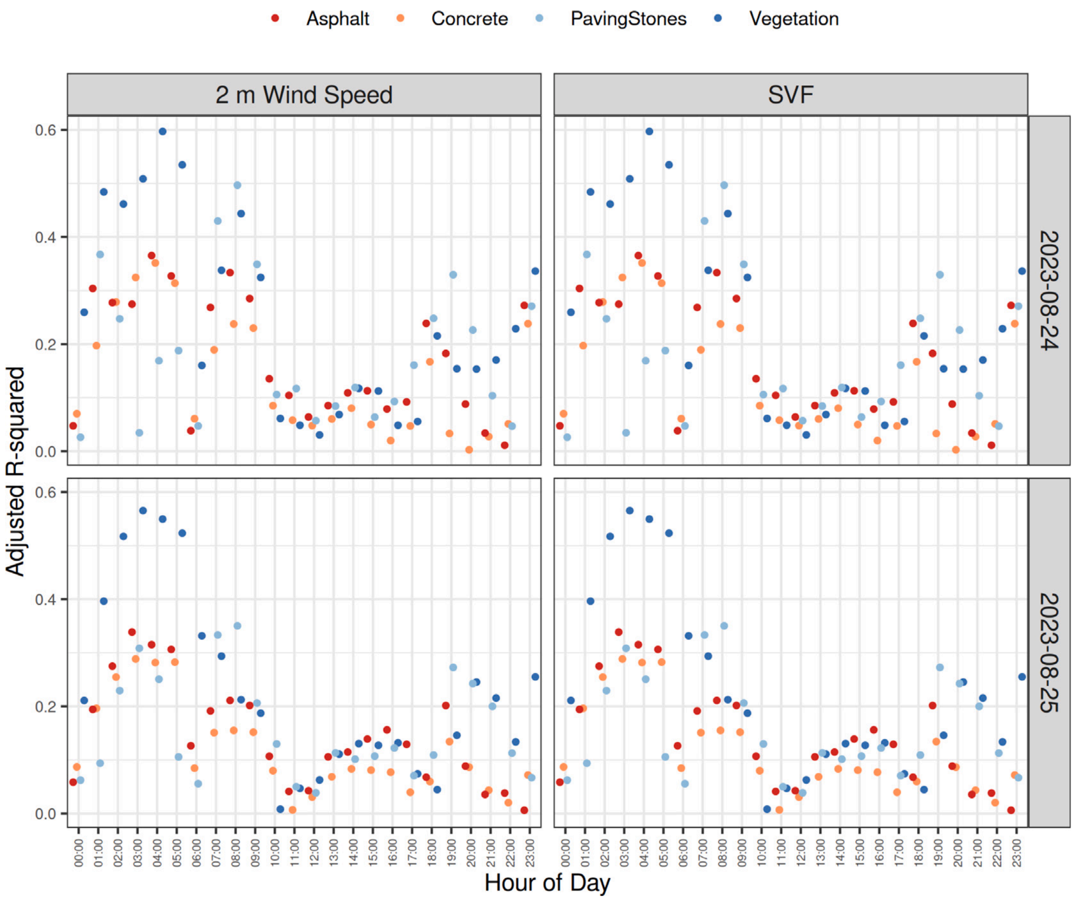

Fig. B.13. Adjusted R-squared values for the hourly and surface-specific multiple linear regression models. Each point represents the adjusted R-squared for a model fitted to data from a specific hour and surface type (Asphalt, Concrete, Paving Stones, Vegetation). Results are shown for two simulated days, August 24 (top panel) and August 25 (bottom panel), 2023. These values indicate the proportion of variance in 2 m air temperature explained by the model, adjusted for the number of predictors.

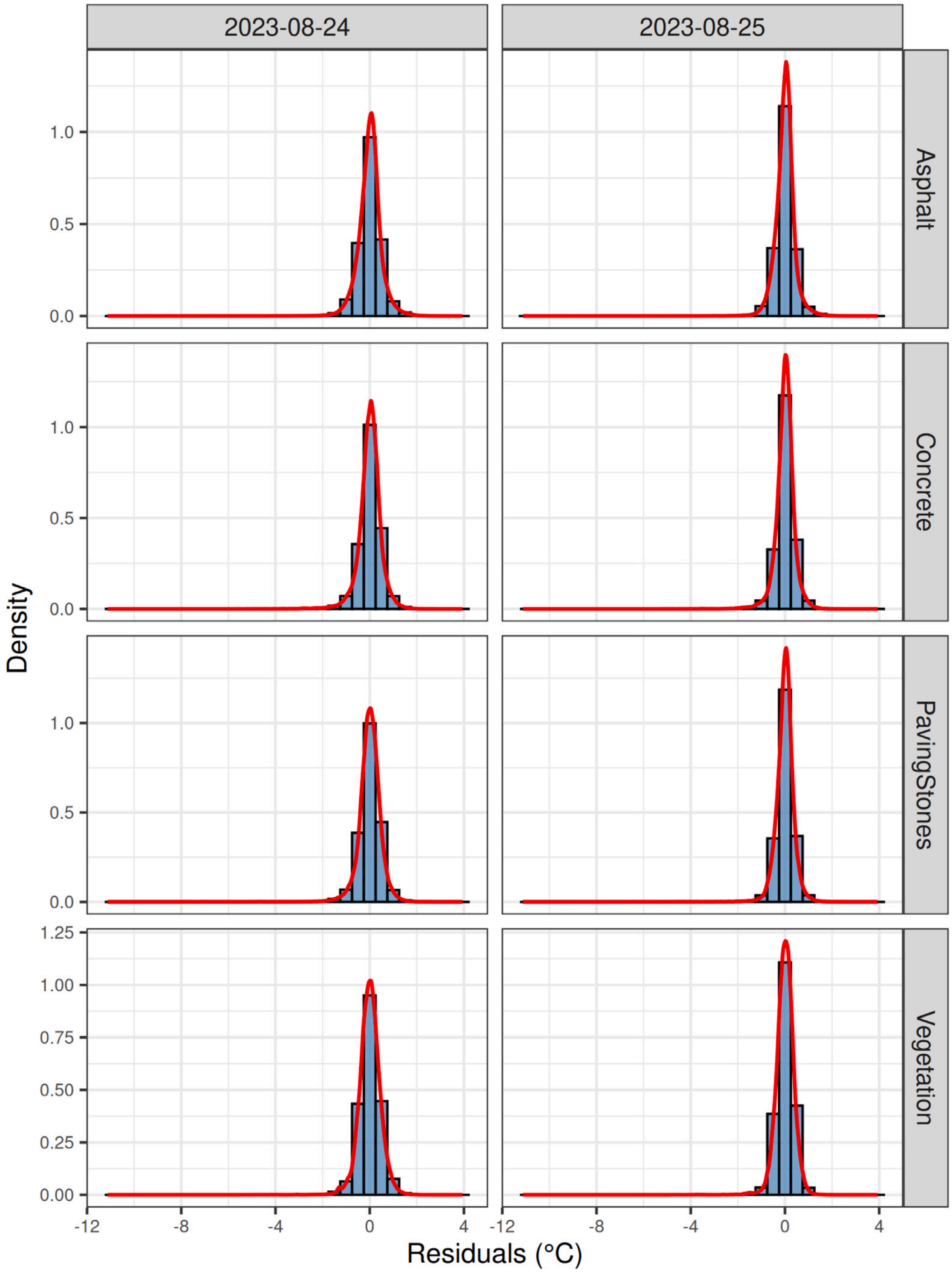

Fig. B.14. Histograms of the residuals (°C) from the hourly and surface-specific multiple linear regression models, aggregated by surface type and day on August 24 (left column) and August 25 (right column), 2023. The red line overlay represents the kernel density estimate of the residual distribution, providing a smoothed representation of the data probability density.

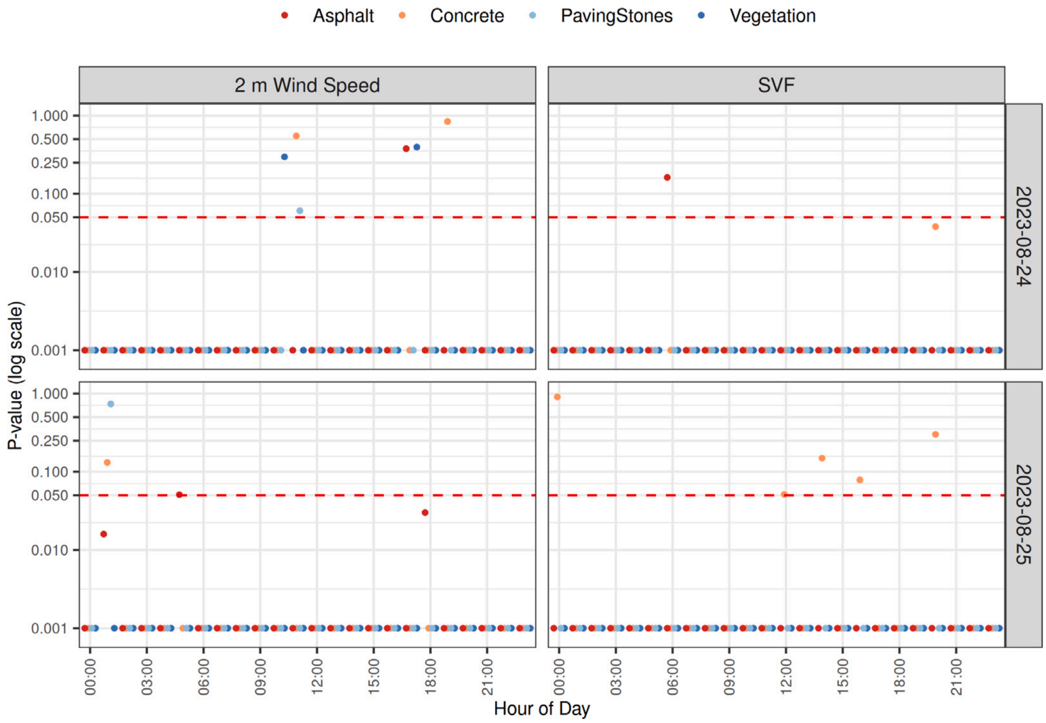

Fig. B.15. P-values (on a logarithmic scale) for the estimated coefficients of 2 m Wind Speed (left column) and Sky View Factor (SVF, right column), derived from the hourly and surface-specific multiple linear regression models. The dashed red line indicates the p = 0.05 significance threshold, with points below this line considered statistically significant. To enhance readability and emphasize values above 0.05, and because computed p-values spanned several orders of magnitude, all p-values below 0.001 are reported as 0.001.

References

Antolini, G., Auteri, L., Pavan, V., Tomei, F., Tomozeiu, R., Marletto, V., 2016. A daily high-resolution gridded climatic data set for Emilia-Romagna, Italy, during 1961–2010. Int. J. Climatol. 36 (4).

Balany, F., Ng, A.W.M., Muttil, N., Muthukumaran, S., Wong, M.S., 2020. Green infrastructure as an urban heat island mitigation strategy—a review. Water 12 (12), 3577.

Baldauf, M., Seifert, A., Förstner, J., Majewski, D., Raschendorfer, M., Reinhardt, T., 2011. Operational convective-scale numerical weather prediction with the COSMO model: Description and sensitivities. Mon. Weather Rev. 139 (12), 3887–3905.

Belda, M., Resler, J., Geletič, J., Krč, P., Maronga, B., Sühring, M., Kurppa, M., Kanani-Sühring, F., Fuka, V., Eben, K., et al., 2020. Sensitivity analysis of the PALM model system 6.0 in the urban environment. Geosci. Model Dev. Discuss. 2020, 1–32.

Briscolini, M., Santangelo, P., 1989. Development of the mask method for incompressible unsteady flows. J. Comput. Phys. 84 (1), 57–75.

Carmeliet, J., Derome, D., 2024. How to beat the heat in cities through urban climate modelling. Nat. Rev. Phys. 6 (1), 2–3.

Cava, D., Mortarini, L., Landi, T.C., Drofa, O., Veratti, G., Fiorillo, E., Giostra, U., de Vargas Brondani, D., 2025. Energy partitioning and air temperature anomalies above urban surfaces: A high-resolution PALM-4U study. Atmosphere 16 (12), 1401.

Crespi, A., Brunetti, M., Lentini, G., Maugeri, M., et al., 2018. 1961–1990 high-resolution monthly precipitation climatologies for Italy. Int. J. Climatol. 38 (2), 878–895.

Daramola, M.T., Balogun, I.A., 2019. Analysis of the urban surface thermal condition based on sky-view factor and vegetation cover. Remote Sens. Appl.: Soc. Environ. 15, 100253.

Davolio, S., Vercellino, M., Miglietta, M.M., Pitura, L.D., Laviola, S., Levizzani, V., 2023. The influence of an atmospheric river on a heavy precipitation event over the western Alps. Weather Clim. Extrem. 39, 100542.

De Benedictis, C., Nardino, M., Cremonini, L., Neri, L., Fiorillo, E., 2025. Quantification of the ecosystem services provided by public and private green in a residential area of Bologna, Northern Italy. Urban Ecosyst. 28 (4), 171.

Deardorff, J.W., 1980. Stratocumulus-capped mixed layers derived from a three-dimensional model. Bound.-Layer Meteorol. 18, 495–527.

Dirksen, M., Ronda, R., Theeuwes, N.E., Pagani, G.A., 2019. Sky view factor calculations and its application in urban heat island studies. Urban Clim. 30, 100498.

Drofa, O., 2025. Pochva: a new hydro-thermal process model in soil, snow, and vegetation for application in atmosphere numerical models. Geosci. Model Dev. 18 (11), 3175–3209.

Gronemeier, T., Inagaki, A., Gryschka, M., Kanda, M., 2015. Large-eddy simulation of an urban canopy using a synthetic turbulence inflow generation method. J. Jpn. Soc. Civ. Eng. Ser. B1 (Hydraul. Eng.) 71 (4), I_43–I_48.

Gronemeier, T., Surm, K., Harms, F., Leitl, B., Maronga, B., Raasch, S., 2021. Evaluation of the dynamic core of the PALM model system 6.0 in a neutrally stratified urban environment: comparison between LES and wind-tunnel experiments. Geosci. Model Dev. 14 (6), 3317–3333.

Heinze, R., Moseley, C., Böske, L.N., Muppa, S.K., Maurer, V., Raasch, S., Stevens, B., 2017. Evaluation of large-eddy simulations forced with mesoscale model output for a multi-week period during a measurement campaign. Atmospheric Chem. Phys. 17 (11), 7083–7109.

Kadasch, E., Sühring, M., Gronemeier, T., Raasch, S., 2021. Mesoscale nesting interface of the PALM model system 6.0. Geosci. Model Dev. 14 (9), 5435–5465.

Kim, Y., Castro, I.P., Xie, Z.-T., 2013. Divergence-free turbulence inflow conditions for large-eddy simulations with incompressible flow solvers. Comput. & Fluids 84, 56–68.

Krč, P., Belda, M., Bureš, M., Eben, K., Geletič, J., Radović, J., Řezníček, H., Resler, J., 2025. PALM-meteo 2.6: Processor of PALM meteorological input data. EGUsphere 2025, 1–32.
Krč, P., Resler, J., Sühring, M., Schubert, S., Salim, M.H., Fuka, V., 2020. Radiative Transfer Model 3.0 integrated into the PALM model system 6.0. Geosci. Model Dev. Discuss. 2020, 1–41.
Kusaka, H., Kondo, H., Kikegawa, Y., Kimura, F., 2001. A simple single-layer urban canopy model for atmospheric models: Comparison with multi-layer and slab models. Bound.-Layer Meteorol. 101, 329–358.
Lalic, B., Mihailovic, D.T., 2004. An empirical relation describing leaf-area density inside the forest for environmental modeling. J. Appl. Meteorol. Climatol. 43 (4), 641–645.
Landi, T.C., Drofa, O., Resci, G., Roccato, F., 2025a. MOLOCH4PALM. http://dx.doi.org/10.82214/Y9XG-CN09, Software.
Landi, T.C., Mortarini, L., Roccato, F., 2025b. MOLOCH–PALM modeling system – PALM-4U implementation over Bologna [Data set]. http://dx.doi.org/10.82214/6AN6-R625.
Lin, D., Khan, B., Katurji, M., Bird, L., Faria, R., Revell, L.E., 2020. WRF4PALM v1. 0: a mesoscale dynamical driver for the microscale PALM model system 6.0. Geosci. Model Dev. Discuss. 2020, 1–37.
Lin, D., Zhang, J., Khan, B., Katurji, M., Revell, L.E., 2023. GEO4PALM v1. 1: an open-source geospatial data processing toolkit for the PALM model system. Geosci. Model Dev. Discuss. 2023, 1–36.
Malguzzi, P., Buzzi, A., Drofa, O., 2011. The meteorological global model GLOBO at the ISAC-CNR of Italy assessment of 1.5 yr of experimental use for medium-range weather forecasts. Weather Forecast. 26 (6), 1045–1055.
Maronga, B., Banzhaf, S., Burmeister, C., Esch, T., Forkel, R., Fröhlich, D., Fuka, V., Gehrke, K.F., Geletič, J., Giersch, S., et al., 2020. Overview of the PALM model system 6.0. Geosci. Model Dev. 13 (3), 1335–1372.
Maronga, B., Gryschka, M., Heinze, R., Hoffmann, F., Kanani-Sühring, F., Keck, M., Ketelsen, K., Letzel, M.O., Sühring, M., Raasch, S., 2015. The Parallelized Large-Eddy Simulation Model (PALM) version 4.0 for atmospheric and oceanic flows: model formulation, recent developments, and future perspectives. Geosci. Model Dev. 8 (8), 2515–2551.
Martilli, A., 2002. Numerical study of urban impact on boundary layer structure: Sensitivity to wind speed, urban morphology, and rural soil moisture. J. Appl. Meteorol. Climatol. 41 (12), 1247–1266.
Martilli, A., Nazarian, N., Krayenhoff, E.S., Lachapelle, J., Lu, J., Rivas, E., Rodriguez-Sanchez, A., Sanchez, B., Santiago, J.L., 2024. WRF-Comfort: simulating microscale variability in outdoor heat stress at the city scale with a mesoscale model. Geosci. Model Dev. 17 (12), 5023–5039.
Masson, V., 2006. Urban surface modeling and the meso-scale impact of cities. Theor. Appl. Climatol. 84, 35–45.
Mills, G., 2014. Urban climatology: History, status and prospects. Urban Clim. 10, 479–489.
Moeng, C.-H., Wyngaard, J.C., 1988. Spectral analysis of large-eddy simulations of the convective boundary layer. J. Atmospheric Sci. 45 (23), 3573–3587.
Monin, A.S., Obukhov, A.M., 1954. Osnovnye zakonomernosti turbulentnogo peremeshivanija v prizemnom sloe atmosfery (Basic laws of turbulent mixing in the atmosphere near the ground). Tr. Geofiz. Inst. SSSR 24 (151), 163–187.
Oh, G., Yang, M., Choi, J.-I., 2024. Large-eddy simulation-based wind and thermal comfort assessment in urban environments. J. Wind Eng. Ind. Aerodyn. 246, 105682.
Pappaccogli, G., Zonato, A., Martilli, A., Buccolieri, R., Lionello, P., 2025. MLUCM BEP+ BEM: An offline one-dimensional Multi-Layer Urban Canopy Model based on the BEP+ BEM scheme. Geosci. Model Dev. 18 (19), 7129–7145.
Radović, J., Belda, M., Resler, J., Eben, K., Bureš, M., Geletič, J., Krč, P., Řezníček, H., Fuka, V., 2024. Challenges of constructing and selecting the "perfect" boundary conditions for the large-eddy simulation model PALM. Geosci. Model Dev. 17 (7), 2901–2927.
Resler, J., Bauerová, P., Belda, M., Bureš, M., Eben, K., Fuka, V., Geletič, J., Jareš, R., Karel, J., Keder, J., et al., 2024. Challenges of high-fidelity air quality modeling in urban environments–PALM sensitivity study during stable conditions. Geosci. Model Dev. 17 (20), 7513–7537.
Rotach, M.W., Gryning, S.-E., Tassone, C., 1996. A two-dimensional Lagrangian stochastic dispersion model for daytime conditions. Q. J. R. Meteorol. Soc. 122 (530), 367–389.
Saiki, E.M., Moeng, C.-H., Sullivan, P.P., 2000. Large-eddy simulation of the stably stratified planetary boundary layer. Bound.-Layer Meteorol. 95 (1), 1–30.
Salamanca, F., Krpo, A., Martilli, A., Clappier, A., 2010. A new building energy model coupled with an urban canopy parameterization for urban climate simulations—part I. formulation, verification, and sensitivity analysis of the model. Theor. Appl. Climatol. 99, 331–344.
Sanchez, B., Santiago, J.L., Martilli, A., Martin, F., Borge, R., Quaassdorff, C., de la Paz, D., 2017. Modelling NOX concentrations through CFD-RANS in an urban hot-spot using high resolution traffic emissions and meteorology from a mesoscale model. Atmos. Environ. 163, 155–165.
Stewart, I.D., Oke, T.R., Krayenhoff, E.S., 2014. Evaluation of the'local climate zone'scheme using temperature observations and model simulations. Int. J. Climatol. 34 (4).
Tominaga, Y., Wang, L.L., Zhai, Z.J., Stathopoulos, T., 2023. Accuracy of CFD simulations in urban aerodynamics and microclimate: Progress and challenges. Build. Environ. 110723.
Unger, J., 2009. Connection between urban heat island and sky view factor approximated by a software tool on a 3D urban database. Int. J. Environ. Pollut. 36 (1–3), 59–80.
Vieira Zezzo, L., Pereira Coltri, P., Dubreuil, V., 2023. Microscale models and urban heat island studies: A systematic review. Environ. Monit. Assess. 195 (11), 1284.
Vogel, J., Stadler, S., Chockalingam, G., Afshari, A., Henning, J., Winkler, M., 2025. SanDyPALM v1. 0: Static and dynamic drivers for the PALM-4U model to facilitate realistic urban microclimate simulations. EGUsphere 2025, 1–48.
Wang, Y., Ma, Y.-F., Muñoz-Esparza, D., Dai, J., Li, C.W.Y., Lichtig, P., Tsang, R.C.-W., Liu, C.-H., Wang, T., Brasseur, G.P., 2023. Coupled mesoscale–microscale modeling of air quality in a polluted city using WRF-LES-Chem. Atmospheric Chem. Phys. 23 (10), 5905–5927.
Wang, C., Zhao, Y., Li, Q., Wang, Z.-H., Fan, J., 2025. Ultrafine-resolution Urban Climate modeling: Resolving processes across scales. J. Adv. Model. Earth Syst. 17 (6), e2025MS005053.
Xie, Z.-T., Castro, I.P., 2008. Efficient generation of inflow conditions for large eddy simulation of street-scale flows. Flow Turbul. Combust. 81 (3), 449–470.
Zampieri, M., 2004. Comparison among first, second and third order CBL models. In: Proc. of the 16th Symposium on Boundary Layers and Turbulence. Portland, ME.
Zhiyin, Y., 2015. Large-eddy simulation: Past, present and the future. Chin. J. Aeronaut. 28 (1), 11–24.
Zonato, A., Martilli, A., Di Sabatino, S., Zardi, D., Giovannini, L., 2020. Evaluating the performance of a novel WUDAPT averaging technique to define urban morphology with mesoscale models. Urban Clim. 31, 100584.